IMMUNOLOGY

NF-κB and TET2 promote macrophage reprogramming in hypoxia that overrides the immunosuppressive effects of the tumor microenvironment

Carlos de la Calle-Fabregat[1,2]*†, Josep Calafell-Segura[1]†, Margaux Gardet[2], Garett Dunsmore[2], Kevin Mulder[2], Laura Ciudad[1], Aymeric Silvin[2], Joaquim Moreno-Càceres[3], Ángel L. Corbí[4], Cristina Muñoz-Pinedo[3], Judith Michels[5,6], Sébastien Gouy[7], Charles-Antoine Dutertre[2], Javier Rodríguez-Ubreva[1], Florent Ginhoux[2], Esteban Ballestar[1,8]*

Macrophages orchestrate tissue homeostasis and immunity. In the tumor microenvironment (TME), macrophage presence is largely associated with poor prognosis because of their reprogramming into immunosuppressive cells. We investigated the effects of hypoxia, a TME-associated feature, on the functional, epigenetic, and transcriptional reprogramming of macrophages and found that hypoxia boosts their immunogenicity. Hypoxic inflammatory macrophages are characterized by a cluster of proinflammatory genes undergoing ten-eleven translocation–mediated DNA demethylation and overexpression. These genes are regulated by NF-κB, while HIF1α dominates the transcriptional reprogramming, demonstrated through ChIP-seq and pharmacological inhibition. In bladder and ovarian carcinomas, hypoxic inflammatory macrophages are enriched in immune-infiltrated tumors, correlating with better patient prognoses. Coculture assays and cell-cell communication analyses support that hypoxic-activated macrophages enhance T cell–mediated responses. The NF-κB–associated hypomethylation signature is displayed by a subset of hypoxic inflammatory macrophages, isolated from ovarian tumors. Our results challenge paradigms regarding the effects of hypoxia on macrophages and highlight actionable target cells to modulate anticancer immune responses.

INTRODUCTION

Macrophages (MACs) are sentinels of the innate immune system whose fundamental functions encompass phagocytosis, antigen presentation, and modulation of neighboring cells (*1*, *2*). Tissue MACs can originate from precursors established during embryogenesis or, alternatively, differentiate from monocytes (MOs) extravasating from the peripheral blood (*3*). Before undergoing differentiation within tissues, MOs migrate into niches characterized by diverse physical and biochemical features (*4*). Within this context, a wide range of interactions between MOs and MACs and their environment shape their phenotype and functions (*5*). These interactions are mediated by a variety of stimuli occurring either sequentially or simultaneously, highlighting the complexity of signaling pathways involved (*6*). Pathological states further influence these interactions, leading to altered MAC functions (*7*). All of these microenvironmental cues, which are specific to tissue and context, have the capacity to modulate MAC phenotype by regulating epigenetic and transcriptional programs (*8*, *9*). Consequently, such signals contribute to the emergence of a heterogeneous range of MACs that coexist in the tissues, with fluctuating proportions in health and disease (*10*).

Oxygen availability influences MAC function in physiological and pathological situations. Hypoxia is a hallmark of multiple diseased contexts, such as solid tumors (*11*), arthritic joints (*12*), or ischemic tissues (*13*), where appropriate oxygen influx is impaired. Exposure to hypoxic conditions induces the stabilization of hypoxia-inducible factors (HIFs), which are responsible for the cellular adaptation to oxygen deprivation. Among others, HIF transcription factors (TFs) regulate genes related to metabolism, nutrient transport, angiogenesis, and cell migration (*14*). HIFs have also been described as regulators of inflammatory processes (*15*). However, the underlying mechanism for this is still controversial, as there is evidence associating HIF activity with both proinflammatory and anti-inflammatory features, depending on cellular and physiological context (*16*–*18*).

Hypoxia has the ability to rewire the epigenetic landscape of cells (*19*, *20*), including MACs (*21*). We and others have demonstrated that DNA methylation, a major epigenetic modification, determines the acquisition of immune features by MACs and other MO-derived cells (*22*, *23*). Such changes in DNA methylation are dependent on context-specific TFs and occur in orchestration with additional epigenetic modifications such as histone marks (*22*, *23*). Under conditions of low oxygen levels, the activity of ten-eleven translocation (TET) methylcytosine dioxygenase enzymes, required for active DNA demethylation (*24*), is hindered (*25*). In the tumor microenvironment (TME), which is commonly characterized by hypoxia (*11*), TET inhibition promotes hypermethylation of tumor suppressor genes in cancer cells, affecting their expression (*26*). Nevertheless, genomic regulation and transcriptional responses induced by hypoxia differ substantially between distinct cell types (*19*, *27*).

[1]Epigenetics and Immune Disease Group, Josep Carreras Leukaemia Research Institute (IJC), 08916 Badalona, Barcelona, Spain. [2]INSERM UMR1015, Gustave Roussy Cancer Campus, 94805 Villejuif, France. [3]Preclinical and Experimental Research in Thoracic Tumors (PReTT), Oncobell Program, Institut d'Investigació Biomèdica de Bellvitge (IDIBELL), 08908 L'Hospitalet de Llobregat, Barcelona, Spain. [4]Myeloid Cell Laboratory, Centro de Investigaciones Biológicas, CSIC, Madrid, Spain. [5]INSERM UMR1186, Integrative Tumor Immunology and Immunotherapy, Gustave Roussy, Faculté de Médecine, Université Paris-Saclay, 94805 Villejuif, France. [6]Département de Médecine Oncologique, Gustave Roussy, 94805 Villejuif, France. [7]Department of Surgical Oncology, Gustave Roussy, 94805 Villejuif, France. [8]Epigenetics in Inflammatory and Metabolic Diseases Laboratory, Health Science Center (HSC), East China Normal University (ECNU), Shanghai 200241, China.
*Corresponding author. Email: carlos.de-la-calle-fabregat@gustaveroussy.fr (C.d.l.C.-F.); eballestar@carrerasresearch.org (E.B.)
†These authors contributed equally to this work.

Although there is evidence linking DNA methylation levels with the immunogenic status of the hypoxic TME (*28*), the direct effect of these alterations on the MAC functions is still unclear. Given the reduced levels of oxygen in the TME and the pivotal role of TET-mediated demethylation for MAC biology, it is likely that hypoxia affects their immunological properties. Moreover, although, in several studies, hypoxia is considered an immunosuppression-associated factor in the TME (*16*, *29*, *30*), the specific effect of oxygen restriction on MACs in this context remains uncertain.

Thus, to study the effect of hypoxia and its role underlying the acquisition of unique phenotypic and molecular features by MACs, we used an in vitro differentiation model from human MOs to MACs in normoxic (21% O_2) and hypoxic (1% O_2) conditions and additionally stimulated them with lipopolysaccharide (LPS) to evaluate their immune activation potential. We then characterized the functional, epigenomic, and transcriptomic profiles of all those conditions. Our results revealed that MACs differentiated and activated under hypoxic conditions (herein named "$mMAC_1$") acquire an enhanced proinflammatory program through a DNA methylation–mediated mechanism. The molecular signatures of $mMAC_1$, characterized by nuclear factor κB (NF-κB)–mediated DNA demethylation and overexpression of proinflammatory activation genes, were similarly found in an in vivo MAC subpopulation, isolated from human tumors, suggesting that $mMAC_1$ potentially corresponds to a subset of bona fide tumor-associated MACs. Notably, tumors with high estimated loads of $mMAC_1$ signature–bearing cells were associated with generally better patient survival. Our results highlight the potential of hypoxia as an enhancer of immunogenic properties in MACs in the TME and identify previously unreported mechanisms mediating this phenomenon, posing a refined understanding of the effect of hypoxia upon MACs in vitro and in vivo.

RESULTS

Hypoxia elicits inflammatory features and NF-κB–associated DNA demethylation in activated MACs

To investigate the impact of hypoxia on the immunological properties of MACs and their associated epigenomic reprogramming, we differentiated in vitro human peripheral blood MOs in the presence of MAC colony-stimulating factor (M-CSF) for 5 days in normoxic (21% O_2) or hypoxic (1% O_2) conditions. In addition, the resulting MACs were treated with LPS for 48 hours to induce their activation/maturation or treated with a vehicle for the same time as a control (Fig. 1A).

Under these conditions, mature hypoxic MACs ($mMAC_1$) produced higher levels of the inflammatory cytokines interleukin-6 (IL-6) and tumor necrosis factor–α (TNF-α) and lower levels of the anti-inflammatory cytokine IL-10 than mature normoxic MACs ($mMAC_{21}$; Fig. 1B). At the cell surface level, $mMAC_1$ expressed higher levels of the major histocompatibility complex (MHC) class II human leukocyte antigen–DR (HLA-DR) and costimulatory proteins CD86 and CD80 than their normoxic counterpart ($mMAC_{21}$), as determined by flow cytometry (Fig. 1C), which is consistent with an enhanced antigen presentation capacity. On the other hand, resting/immunoregulatory MAC surface proteins CD14, CD206, and CD163 were decreased in $mMAC_1$ versus $mMAC_{21}$, suggesting a phenotypic switch of these cells to a less anti-inflammatory phenotype. Hypoxic cells, both at steady state and after activation, displayed a decreased capacity to suppress $CD8^+$ T cell proliferation than normoxic cells in a coculture assay (Fig. 1D and fig. S1A). All these results suggest that hypoxia increases the proimmunogenic functions of MACs.

To study the effect of hypoxia on the epigenomic landscape of MACs, we then performed DNA methylation profiling using Illumina Infinium MethylationEPIC arrays. Comparison among conditions revealed a substantial number of differentially methylated positions [DMPs; false discovery rate (FDR) < 0.05 and absolute $\Delta\beta > 0.2$; see Supplementary Methods] among the different conditions (Fig. 1E, fig. S1B, and table S1A). Specifically, we identified DMPs grouped into three different clusters: cluster C1 (2782 CpGs), C2 (403 CpGs), and C3 (903 CpGs; table S1B). Clusters C1 and C3 corresponded with hypomethylated and hypermethylated CpG sites, respectively, in normoxic MACs when compared to MOs. In these clusters, the methylation tendency was partially inhibited in hypoxia. On the other hand, cluster C2 displayed a marked hypomethylation specifically in mature hypoxic MACs ($mMAC_1$; Fig. 1E and fig. S1B) in comparison with mature normoxic MACs ($mMAC_{21}$).

DMPs in cluster C1, the largest cluster, displayed a tendency consistent with an inhibition of DNA demethylation under hypoxic conditions, as observed in (*26*), and were enriched in motifs of the activator protein 1 (AP-1) complex, canonically associated with MAC differentiation (Fig. 1F). Similarly, DMPs in cluster C3, which were also enriched in motifs associated with myeloid cell differentiation, such as those in those in the Runt-related (RUNX) and E26 transformation-specific (ETS) transcription factor families (*31*), displayed hypoxia-associated inhibition of the hypermethylation observed for MACs in normoxia. In contrast, DMPs in cluster C2 displayed hypoxia-associated demethylation specific to activated MACs and were highly enriched in motifs of the NF-κB family, classically associated with Toll-like receptor signaling (*32*), among others (Fig. 1F). Specific examples of demethylated CpGs in cluster C2 included those in the loci of genes such as *IL6* and *TNF* (fig. S1C), which is consistent with the increased levels of their products in the supernatant of $mMAC_1$ (Fig. 1B).

To characterize the DMP clusters from a genomic standpoint, we annotated them in genomic and CpG context categories. DMPs in clusters C1 to C3, particularly those in cluster C2, were enriched in intergenic and open sea regions (fig. S1D). In addition, reanalysis of public MAC histone mark chromatin immunoprecipitation followed by sequencing (ChIP-seq) data (see Supplementary Methods) revealed that cluster C2 regions gain canonical enhancer (H3K4me1) and enhancer activation (H3K27ac) histone marks after activation in normoxic conditions (fig. S1E), suggesting that C2 regions consist of LPS-dependent de novo enhancers (*33*). Cluster C2 DMPs also displayed the highest enrichment for human MO enhancer chromatin state, defined by combinations of different histone marks (see Supplementary Methods) (*34*). These results are consistent with the usual observation that DNA methylation–dynamic genomic regions are associated with distal regulatory elements (*35*).

All these results indicate that hypoxic MACs display a more proinflammatory phenotype compared with their normoxic counterparts. In addition, hypoxia partially blocks the DNA methylation changes associated with MAC differentiation in normoxic conditions. Last, LPS induces specific NF-κB–associated demethylation in inflammatory genes and enhancers in hypoxic conditions that might contribute to the more proinflammatory phenotype observed in hypoxic MACs.

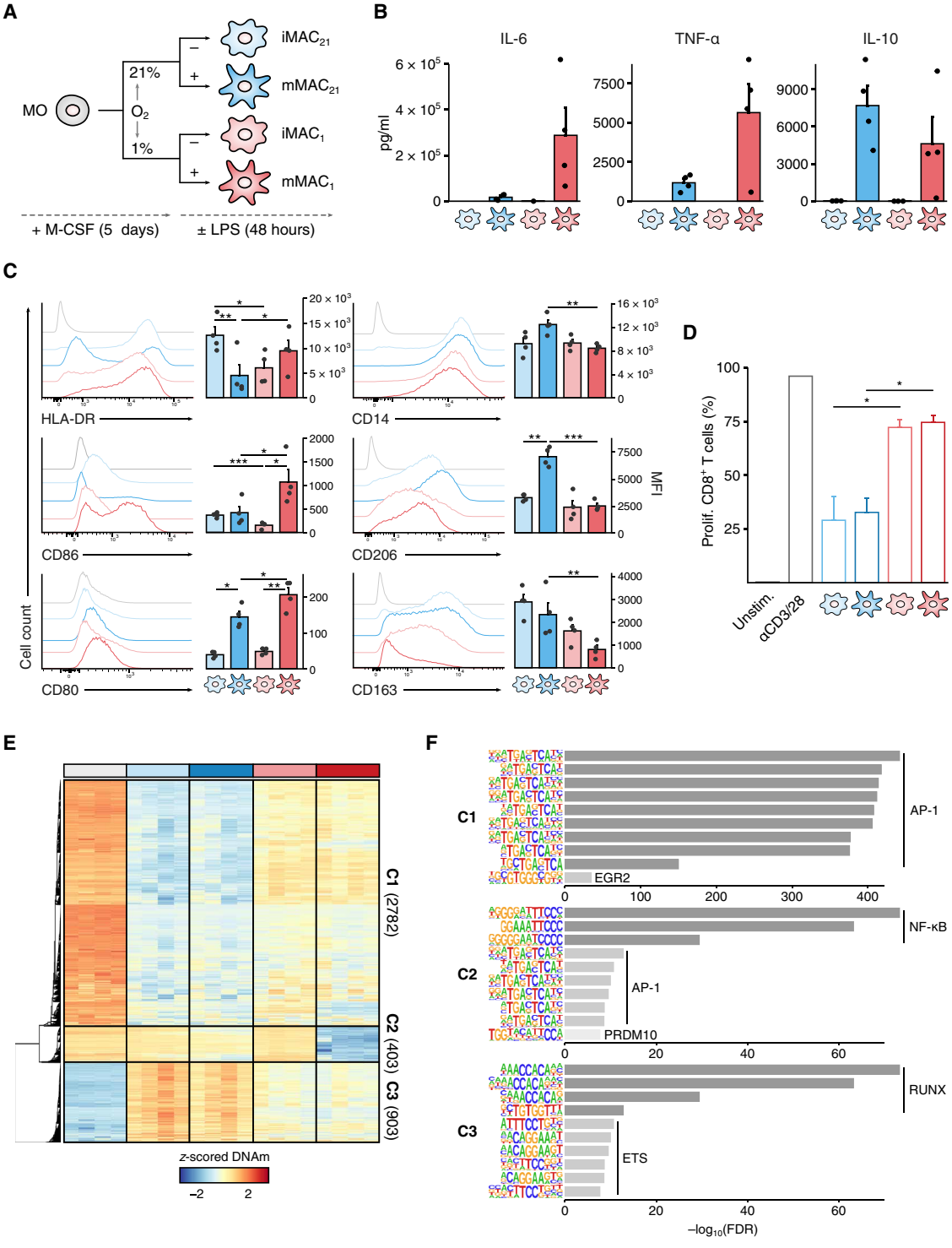

Fig. 1. Phenotypic, functional, and DNA methylation characterization of MAC differentiation and activation in normoxia and hypoxia. (**A**) Scheme depicting the in vitro differentiation system. (**B**) Cytokine (IL-6, TNF-α, and IL-10) concentrations in cell culture supernatants, quantified by enzyme-linked immunosorbent assay ($n = 4$). (**C**) Analysis of cell surface protein expression, quantified in MACs by flow cytometry. Left: Fluorescence histograms of concatenated replicates ($n = 4$). Right: Histograms showing mean fluorescence intensities (MFIs) of the same replicates. (**D**) $CD8^+$ T cell proliferation [i.e., percent of cells with decreased carboxyfluorescein succinimidyl ester (CFSE) staining] in the presence or absence of allogeneic MACs ($n = 4$). First bar: Negative control [no MACs and no T cell receptor (TCR) stimulation]; second bar: positive control (no MACs and TCR stimulation); bars three to six: coculture with MACs and TCR stimulation. (**E**) Heatmap depicting differential DNA methylation analysis results, aggregated in three different clusters (C1 to C3). Blue and red indicate lower and higher methylation, respectively. (**F**) Top 10 most significantly enriched TF motifs in the three different cluster regions, identified by HOMER. DNAm, DNA methylation. $*P < 0.05$, $**P < 0.01$, $***P < 0.001$.

Hypoxia-induced transcriptomic reprogramming to proinflammatory MACs mainly depends on HIF1α and NF-κB

Next, we analyzed the transcriptome of MACs in all the aforementioned conditions using bulk RNA sequencing (RNA-seq). We identified four different clusters (E1 to E4) comprising a total of 3737 differentially expressed genes (DEGs; FDR < 0.05 and absolute $\log_2$ fold change >1; see Supplementary Methods and Fig. 2A and table S2, A and B). E1 (233 DEGs) corresponds to genes up-regulated in hypoxic MACs ($iMAC_1$ and $mMAC_1$). E2 (1452 DEGs) is composed of genes that are up-regulated in activated MACs ($mMAC_{21}$ and $mMAC_1$) with a more marked increase in $mMAC_1$. E3 (732 DEGs) includes genes that become down-regulated in hypoxia ($iMAC_1$ and $mMAC_1$), which further down-regulate in $mMAC_1$. Last, E4 (1330 DEGs) corresponds to genes that are down-regulated upon activation. Gene ontology (GO) analysis of E1 to E4 clusters revealed an enrichment in functional categories associated with a variety of immune functions (Fig. 2B). In particular, the E2 cluster (up-regulated after activation) was enriched in categories related to response to interferons (IFNs), LPS, and TNF-α, as well as positive regulation of NF-κB (Fig. 2B), consistent with the association of this factor in genes that are demethylated specifically in $mMAC_1$ (Fig. 1F).

When evaluating significant DEGs in MACs across pairwise comparisons, we identified that differences in expression differed more markedly along the hypoxia axis ($iMAC_{21}$ versus $iMAC_1$ and $mMAC_{21}$ versus $mMAC_1$) than along the LPS axis ($iMAC_{21}$ versus $mMAC_{21}$ and $iMAC_1$ versus $mMAC_1$), suggesting that the transcriptional program elicited by hypoxia diverges between resting and activated MACs, whereas the core LPS-response program is more conserved between normoxia and hypoxia (Fig. 2C). LPS in hypoxia induced a higher amount of DEGs (Fig. 2C), and in a principal components analysis (PCA) of the most variable genes, $mMAC_1$ was the most segregated condition among all MACs across PC2, which explains gene expression variance induced by the activation (fig. S2A). In this analysis, activated MACs ($mMAC_{21}$ and $mMAC_1$) appear far more separated among themselves than unstimulated MACs ($iMAC_{21}$ and $iMAC_1$), which highlights that the greatest differences between normoxia and hypoxia are reached after LPS activation (fig. S2A).

Cluster C2–associated genes were specifically enriched within cluster E2, calculated by a Fisher's exact test (Fig. 2, A and D), and were significantly associated with genes up-regulated after LPS stimulation (either in normoxia or hypoxia, fig. S2B) and with up-regulated genes between $mMAC_{21}$ and $mMAC_1$ in a gene set enrichment analysis (GSEA; Fig. 2E).

To link the identified transcriptional differences with the involvement of specific TFs, we estimated TF activity by discriminant regulon expression analysis (DoRothEA) (*36*). By performing this analysis in each comparison along the hypoxia axis, we observed that HIF1A was the most enriched TF regulon in the $iMAC_{21}$ versus $iMAC_1$ comparison. However, after comparing the two activated conditions ($mMAC_{21}$ versus $mMAC_1$), HIF1A was overcome by signal transducer and activator of transcription 2 (STAT2) and interferon regulatory factor 1 (IRF1) regulon scores, suggesting a strong inflammatory and IFN signaling activation besides the hypoxic induction in $mMAC_1$ (Fig. 2F). The RELA (encoding the p65 subunit of the canonical NF-κB complex) regulon was also significantly activated in hypoxic conditions, although to a greater extent in the LPS-activated conditions [normalized enrichment score (NES) = 3.8 in $iMAC_{21}$ versus $iMAC_1$; 5 in $mMAC_{21}$ versus $mMAC_1$], which highlights that hypoxia also induces inflammatory activation in MACs (Fig. 2F). On the other hand, reanalysis of RNA-seq data of MACs activated with LPS in a time-course manner (*37*) revealed that LPS stimulation promotes the up-regulation of HIF1α transcriptional targets at late time points (4 to 12 hours after LPS; fig. S2C). However, DMPs in C2 were preferentially associated with genes that up-regulate at early time points (0.5 and 2 hours) after LPS stimulation, which are predominantly associated with NF-κB activity (fig. S2, D and C).

Next, we decided to resolve whether the observed hypoxia-specific DNA demethylation and transcriptional overexpression during activation (summarized by selected examples depicted in Fig. 2G) were exclusive to LPS stimulation or also generalizable to other activating signals. With that aim, we stimulated MAC_{21} and MAC_1 with different NF-κB–activating ligands for 48 hours and measured mRNA expression of the genes in Fig. 2G (table S3). Stimulation with pathogen-associated molecular pattern (PAMP) LPS, Pam3-Cys (P3C), CpG, poly I:C, and cytokines TNF-α and IL-1β induced increased expression of inflammatory genes in hypoxia as compared to normoxia, in most cases (fig. S2E), suggesting that NF-κB overactivation, rather than a particular stimulus, is responsible for the up-regulation of inflammatory genes in hypoxic MACs. Last, we wondered whether the changes observed during the activation in hypoxia require that the differentiation process from MO to MAC also takes place in hypoxic conditions. To interrogate this question, we differentiated and activated the cells as described originally [under normoxic and hypoxic conditions during the entire differentiation and activation process (Fig. 1A), i.e., "canonical" conditions] or by swapping the samples from normoxia to hypoxia and vice versa before the activation step (i.e., "swap" conditions; fig. S2F), and we measured the expression of genes in Fig. 2G in a time-course manner. The results from this analysis first confirmed the differences after LPS activation between canonical normoxic and hypoxic conditions and revealed that the most significant differences occur at shorter time points (2 hours after LPS stimulation; fig. S2G, line plots). In addition, swapping MACs from normoxia to hypoxia 2 hours before activation with LPS proved to be sufficient to increase expression equaling canonical hypoxia levels, and vice versa (fig. S2G, bar plots). This suggests that LPS activation in hypoxia is sufficient to boost gene expression of inflammatory genes independently of oxygen levels during differentiation, in line with our previous findings (*38*).

Together, these results indicate that inflammatory activation of MACs in hypoxia in vitro boosts the expression of proinflammatory genes associated with demethylated DNA regions, a process that involves activation of HIF1α and NF-κB alongside additional inflammatory TFs.

Hypoxia and LPS activate shared and independent transcriptional programs

To understand the participation of HIF1α and NF-κB during the reprogramming of MACs in hypoxia, we analyzed the protein levels of HIF1α and p65 over time before and after activation using Western blot. Both LPS-mediated activation and hypoxia resulted in increased HIF1α detection, independently, although its maximum was reached at 2 hours after LPS in hypoxia (Fig. 3A and fig. S3A). p65 protein

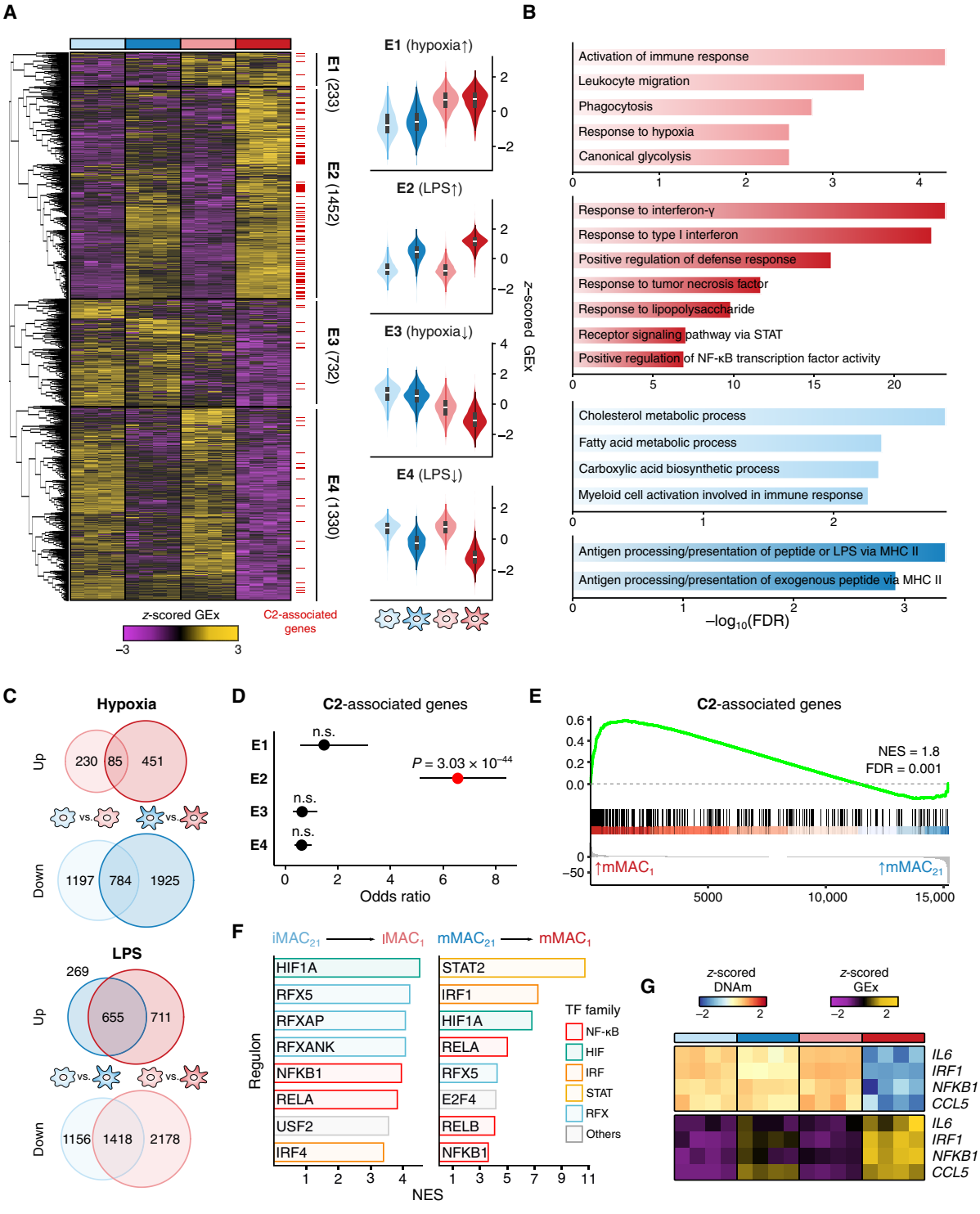

Fig. 2. Analysis of the transcriptional response to inflammatory activation of MACs in hypoxia. (**A**) Heatmap depicting differential mRNA expression results aggregated in four different clusters (E1 to E4). Genes associated to hypoxic-related demethylation (cluster C2) are highlighted with red dashes at the right. Violin plots summarize the distribution of normalized gene expression in every cluster. (**B**) Top significant GO categories for every cluster. (**C**) Overlap between DEGs rendered by comparing different experimental conditions, summarized by Venn diagrams. Comparisons are distributed along the hypoxia axis (considering "up" DEGs as up-regulated in hypoxia) or the LPS axis (considering "up" DEGs as up-regulated in LPS). (**D**) Enrichment of genes in E1 to E4 coinciding with genes associated to cluster C2 calculated by a Fisher's exact test. (**E**) Gene set enrichment analysis (GSEA) of C2-associated genes on $mMAC_1$ (red) versus $mMAC_{21}$ (blue) comparison. (**F**) TF activity inferred by discriminant regulon expression analysis (DoRothEA). Top eight positive (i.e., higher activity in hypoxia) regulons (ordered by NES/FDR) are depicted and colored by TF family in every comparison. (**G**) Selected examples of CpGs in C2 associated to genes up-regulated in $mMAC_1$ versus $mMAC_{21}$. GEx, RNA expression; DNAm, DNA methylation. n.s., not significant.

was induced during activation to comparable levels in MAC_{21} and MAC_1, although there was a slightly higher tendency of expression ($P > 0.05$) in MAC_1 at 2 hours after LPS (Fig. 3A and fig. S3A). To ascertain the subcellular localization dynamics of these proteins throughout this process, we performed immunofluorescence of MAC_{21} and MAC_1 treated with vehicle or LPS for 2 hours (Fig. 3B). HIF1α protein was increased in hypoxia both in the cytoplasm and the nucleus, whereas p65 was increased in the cytoplasm in hypoxic conditions and increased in the nuclei after activation (Fig. 3, B and C). The effect of LPS on subcellular localization was inverse for HIF1α (relative increase in the cytoplasm) and p65 (relative increase in the nucleus), suggesting different molecular mechanisms for the expression/stabilization of both TFs (fig. S3B). The condition showing higher absolute expression of both TFs was $mMAC_1$ (fig. S3B), which reinforces the existence of co-regulatory mechanisms among both TFs in inflammatory hypoxic conditions.

Accordingly, the concomitant effect of hypoxia and activation was also confirmed at the transcriptional level, as both hypoxia and LPS induced the up-regulation of a common set of genes independently (Fig. 3D). Consistent with this, genes in the regulon of HIF1A were up-regulated both in $mMAC_{21}$ and $iMAC_1$ at comparable levels, and their expression reached a maximum in $mMAC_1$; RELA regulon genes were increased in both LPS-activated conditions, with maximum expression in $mMAC_1$ (Fig. 3E). The increased HIF1A regulon expression was driven by the up-regulation of different sets of genes in $mMAC_{21}$ and $iMAC_1$ (fig. S3C and table S2C), suggesting distinct transcriptional programs activated by HIF1α under different conditions. On the contrary, RELA regulon differences were attributable almost exclusively to a hypoxic boosting of genes that were already up-regulated in normoxia (fig. S3C). Overall, these data suggest that hypoxia and LPS activate intersecting mechanisms.

HIF1α and NF-κB transcriptionally co-regulate MAC hypoxic activation

To shed light on the transcriptional regulation by HIF1α and NF-κB in the differentiation and activation of hypoxic MACs, we performed ChIP-seq using antibodies against HIF1α and p65 in all MAC conditions. We consolidated a list of consensus peaks for each condition (table S4, A to D, and Supplementary Methods). Unsupervised clustering of the differentially bound consensus peaks with increased signal either along the hypoxia axis (21% versus 1% of O_2) or the LPS axis (± LPS) led to the identification of three independent clusters (H1 to H3) for HIF1α (Fig. 4A and Supplementary Methods). H1 contains HIF1α peaks that increase binding in hypoxia ($iMAC_1$ or $mMAC_1$); H2 includes HIF1α peaks with increased binding after activation ($mMAC_{21}$ or $mMAC_1$), and H3 consists of HIF1α peaks that increase under hypoxia, activation, or both simultaneously ($iMAC_1$, $mMAC_{21}$, or $mMAC_1$). p65 ChIP-seq peaks revealed one single tendency (P1), showing maximum binding strength in $mMAC_1$, followed by $mMAC_{21}$ (Fig. 4A and table S4E). Of note, in $mMAC_1$, we observed a number of overlapping peaks in clusters of both TF ChIP-seq, which varied for every HIF1α cluster (Fig. 4B). The most significantly enriched

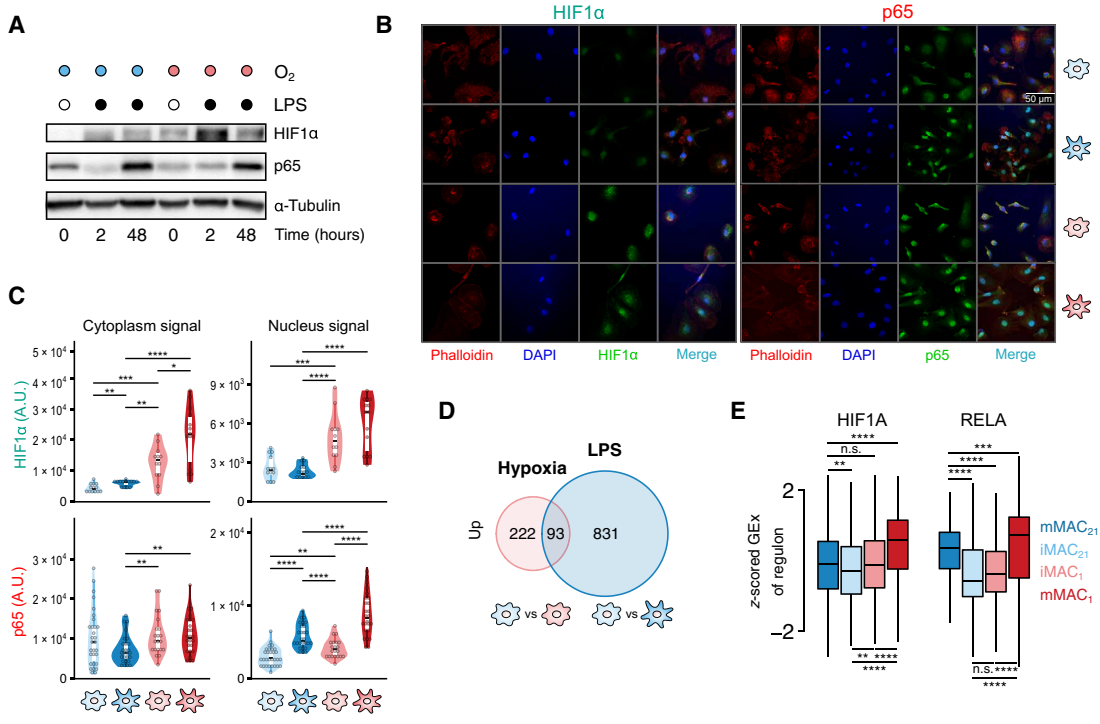

Fig. 3. Mechanistic interplay between HIF1α and p65 under hypoxia and activation. (**A**) Representative Western blot image of HIF1α and p65 in a time course after LPS stimulation in whole cell lysates. α-Tubulin was used as a loading control. (**B**) Immunofluorescence of HIF1α and p65 in MACs at 2 hours after LPS stimulation. Representative images of MAC cultures with fluorescent staining for cytoplasm (phalloidin Alexa Fluor 568, red), nucleus [4′,6-diamidino-2-phenylindole (DAPI), blue], and HIF1α or p65 (Alexa Fluor 488; green; $n = 2$). (**C**) Quantification of immunofluorescence staining signal in the cytoplasm and nucleus of HIF1α and p65 2 hours after LPS stimulation or vehicle. (**D**) Overlap between hypoxia–up-regulated and LPS–up-regulated DEGs. (**E**) Scaled mRNA expression of genes contained in the HIF1A and RELA regulons (DoRothEA regulons, only positive targets). A.U., arbitrary units; GEx, RNA expression. *$P < 0.05$, **$P < 0.01$, ***$P < 0.001$, and ****$P < 0.0001$. n.s., not significant.

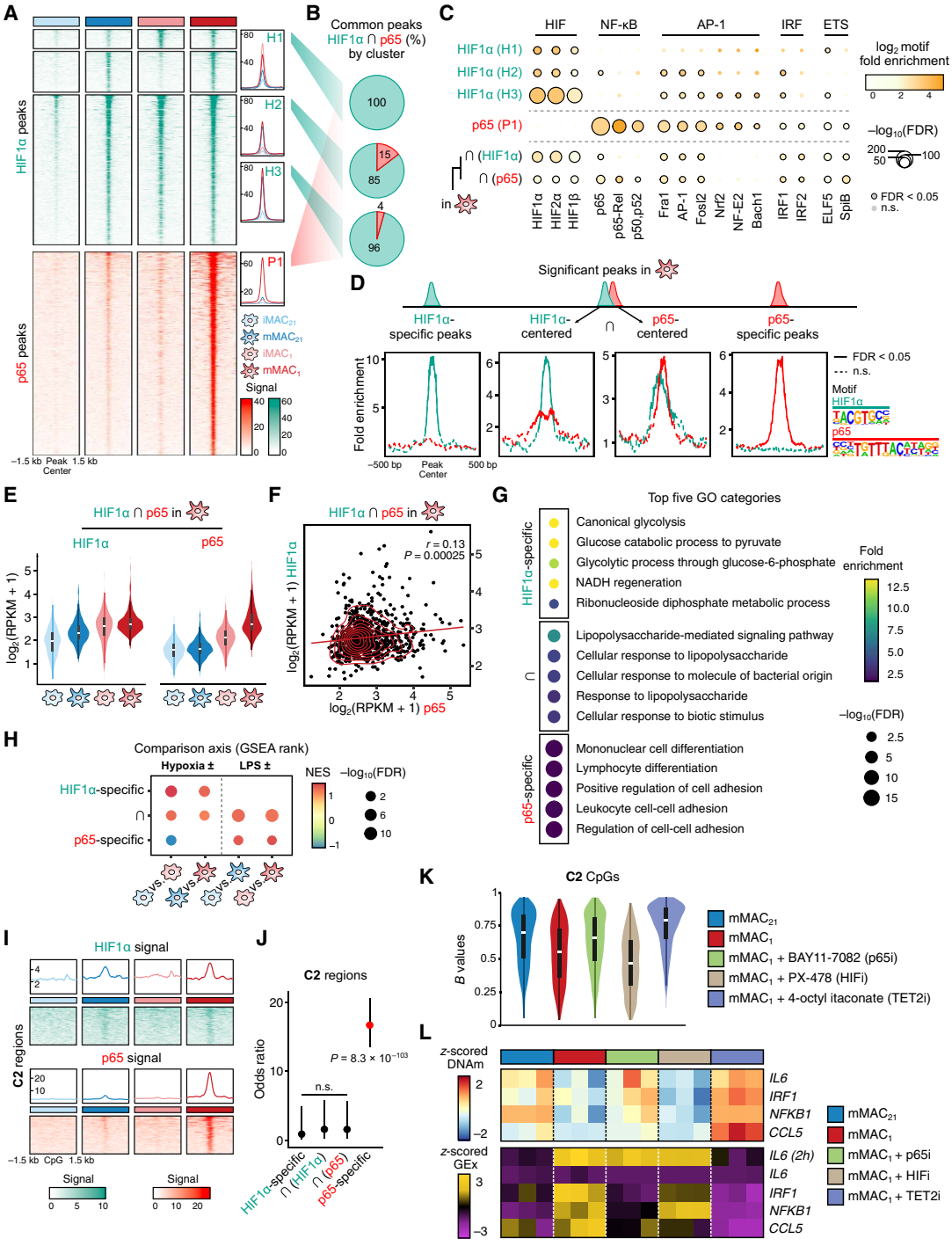

Fig. 4. Binding profiles of HIF1α and p65 on MACs under different conditions. (**A**) Profile plots depicting binding of HIF1α (green, top) or p65 (orange, bottom) binding surrounding each ChIP-seq peak summit. Peaks are clustered in different sets (H1 to H3 for HIF1α and P1 for p65), and the binding signal average of every condition is summarized in respective enrichment plots, on the right. (**B**) Venn diagrams showing overlaps between HIF1α and p65 significant peaks in $mMAC_1$, by cluster. (**C**) Motif enrichment across ChIP-seq peak sets. HIF1α and p65 peaks are shown, along with commonly bound peaks by both TFs in $mMAC_1$. Commonly bound peak enrichment is calculated in a HIF1α- or p65-centered manner. (**D**) Enrichment of HIF1α and p65 motifs around specific and commonly bound peaks in a window of 1 kb flanking the peak summit. (**E**) Normalized HIF1α and p65 ChIP-seq binding signal on commonly bound peaks. (**F**) Correlation between HIF1α and p65 binding signal on commonly bound peaks. (**G**) Top five GO categories enriched in genes with HIF1α peaks only, p65 peaks only, or commonly bound peaks in $mMAC_1$. (**H**) GSEA of genes only bound by HIF1α or p65 or genes with commonly bound peaks on $mMAC_1$ on different comparisons distributed along the hypoxia axis or the LPS axis. (**I**) HIF1α and p65 ChIP-seq signal in windows flanking CpG coordinates from cluster C2. (**J**) Enrichment of peak sets overlapping with CpGs in C2 calculated by a Fisher's exact test. (**K**) Violin plots depicting unscaled *B* values of C2 cluster in $mMAC_{21}$ and $mMAC_1$ untreated or pretreated with p65 inhibitor (BAY11-7082), HIF inhibitor (PX-478), or TET inhibitor (4-octyl itaconate; $n = 3$). (**L**) Scaled DNA methylation and mRNA expression of selected genes from Fig. 2G upon treatment with inhibitors or vehicle. DNAm, DNA methylation; GEx, RNA expression. n.s., not significant.

motifs for HIF1α clusters were HIF and ETS in H1 and AP-1 and IRF in H2-H3 (Fig. 4C). The p65 motif was also significantly enriched in HIF1α cluster H2, which showed the highest overlap with p65 peaks (~15%) in $mMAC_1$ (Fig. 4B). Peaks bound by both HIF1α and p65 in $mMAC_1$ ("∩") revealed a significant enrichment of HIF, NF-κB, AP-1, IRF, and ETS motifs, either centering the analysis on the HIF1α or the p65 binding sites (Fig. 4C and Supplementary Methods).

We next aimed to ascertain whether the concomitant binding of both TFs in the same regions was driven mainly by HIF1α or p65. To do this, first, we calculated the enrichment of the binding motifs of both TFs in a 1–kb window around the centers of peaks specifically bound by HIF1α ("HIF1α-specific") or p65 ("p65-specific") or those commonly bound by both proteins in $mMAC_1$ ("∩"). In cobound peaks, the analysis was performed in a HIF1α-centered or a p65-centered manner. When applied to cobound peaks, the HIF1α-centered analysis revealed a predominance of the HIF1α motif, along with a significant, albeit notably lower, enrichment of the p65 motif (Fig. 4D). On the other hand, the p65-centered analysis revealed similar levels of enrichment for both the p65 and HIF1α motifs (Fig. 4D), suggesting a predominance of HIF1α motifs in these peaks. p65 and HIF1α common peaks displayed a binding profile similar to those that are HIF1α specific, both in terms of gene feature distribution (fig. S4A) and distance to transcription start sites (fig. S4B).

To establish the activation sequence of the cobound TFs (HIF1α and p65) in time, we plotted their binding intensity across all conditions (Fig. 4E). This inspection revealed that although p65 binding mainly increases after activation in hypoxia ($mMAC_1$), HIF1α binding is notably elevated in the hypoxic steady state ($iMAC_1$), suggesting a prior activation of HIF1α over p65 on commonly bound regions. Examples of common peaks showing this tendency are depicted in fig. S4C. However, although statistically significant ($P = 2.5 \times 10^{-4}$), the intensity of binding of both TFs in $mMAC_1$ common peaks did not show a clear linear correlation (Pearson's $r = 0.13$; Fig. 4F), suggesting a cooperation mechanism that is independent of a physical interaction among HIF1α and p65 proteins.

GO analysis of genes bound only by single-TF peaks (either HIF1α or p65) or bearing commonly bound peaks in $mMAC_1$ revealed enrichment in categories related to functionally distinct processes (Fig. 4G). HIF1α-only bound genes were mainly associated with categories related to glycolytic metabolism; p65-only bound genes were associated with immune cell differentiation and adhesion, and genes with cobinding peaks were predominantly associated with the LPS-mediated signaling pathway (Fig. 4G).

Last, to elucidate the effect of TF binding on transcriptional expression, we performed GSEA of genes associated with each ChIP peak set on DEG comparisons. DEG comparisons were distributed along the hypoxia or the LPS axis, as detailed before. Of note, HIF1α- and p65-bound genes were up-regulated significantly only by hypoxia or LPS, respectively, whereas genes with cobinding peaks showed up-regulation independently by either of the two challenges (Fig. 4H). MACs differentiated in hypoxia but unstimulated with LPS ($iMAC_1$) showed a significant down-regulation of p65-bound genes (Fig. 4H), which suggests an inflammatory suppression of these cells, possibly because of an incomplete differentiation process in hypoxic conditions (Fig. 1E and fig. S1B). This highlights a possible paradoxical role of hypoxia depending on the cellular context (e.g., presence or absence of an inflammatory insult), in agreement with previous studies (*39*).

Hypoxia-specific proinflammatory properties of activated MACs are NF-κB– and TET-mediated DNA demethylation dependent

To determine the relationship between HIF1α and p65 binding and hypoxia-specific DNA demethylation, we first plotted the ChIP-seq signal around the coordinates of CpGs in cluster C2 (Fig. 4I). C2 regions were characterized by a strong p65 signal in $mMAC_1$, whereas the HIF1α signal was not notably high in any of the conditions. This was further confirmed by measuring the coincidence between coordinates of ChIP-seq peak sets and C2 CpGs, which revealed that C2 regions are exclusively associated with p65-specific peaks (Fig. 4J).

We then sought to establish the molecular dependency of the demethylation of cluster C2 on HIF1α or p65. To this end, we treated MAC_{21} or MAC_1 with the chemical compounds BAY11-7082 (p65 inhibitor) or PX-478 (HIF1α inhibitor) for 3 hours before LPS stimulation. We also included 4-octyl itaconate, a strong TET2 inhibitor (*40*), as a positive control for the inhibition of active DNA demethylation. Then, we activated MAC_1 with LPS for 48 hours and measured DNA methylation using microarrays. This revealed that inhibition of p65 alone (but not of HIF1α alone) was able to hamper DNA demethylation in hypoxia, which appeared at levels comparable to those of MAC_{21} (Fig. 4K). In those same samples, we also measured the mRNA expression in a representative set of C2-associated genes (depicted in Fig. 2G). As expected, p65 inhibition led to a decreased gene expression of its targets (Fig. 4L). Similarly, samples treated with 4-octyl itaconate showed particularly high DNA methylation levels, as well as decreased mRNA expression, suggesting that DNA methylation is determinant in regulating the expression of these proinflammatory genes (Fig. 4L). HIF1α inhibition, instead, partially reduced the expression of some of these genes, suggesting the existence of additional potential mechanisms associated with the regulation of this factor.

The hypoxic inflammatory MAC signature is found in vivo in human cancers and correlates with T cell presence

We then sought to ascertain the biological relevance of our in vitro–derived signatures in a more physiological context by using public data of in vivo human tissue MACs (*10*). To this end, first of all, we defined specific signature genes for all our experimental conditions (table S5 and Supplementary Methods). C2-associated genes appeared preferentially enriched in the $mMAC_1$-specific signature cluster (Fig. 5A, red dashes). For characterization purposes, we also analyzed TF regulons associated with every population's marker genes by DoRothEA (Fig. 5A, right). Next, we transposed those signatures into the MoMac-VERSE (*10*), which consists of a human MO/MAC atlas comprising 13 different tissues in health and disease, analyzed by single-cell RNA-seq (scRNA-seq). With this approach, we identified an enrichment of $mMAC_1$ gene expression signature, as well as $mMAC_1$-specific DNA demethylation signature (C2-associated genes) on three tissue MO/MAC populations, previously annotated in the MoMac-VERSE: clusters #15 (IL1B Mo), #6 (IL4I1 Mac), and #4 (ISG Mo; Fig. 5B and fig. S5A). In addition, we selected MoMac-VERSE MAC clusters that were not enriched in $mMAC_1$ signatures (i.e., #2 HES1/FOLR2 Mac and #3 TREM2 Mac) to use them as negative controls in further analyses (fig. S5A). Some of these populations (i.e., IL1B Mo, IL4I1 Mac, and TREM2 Mac) were found to be expanded in pathological conditions, such as cancer (*10*).

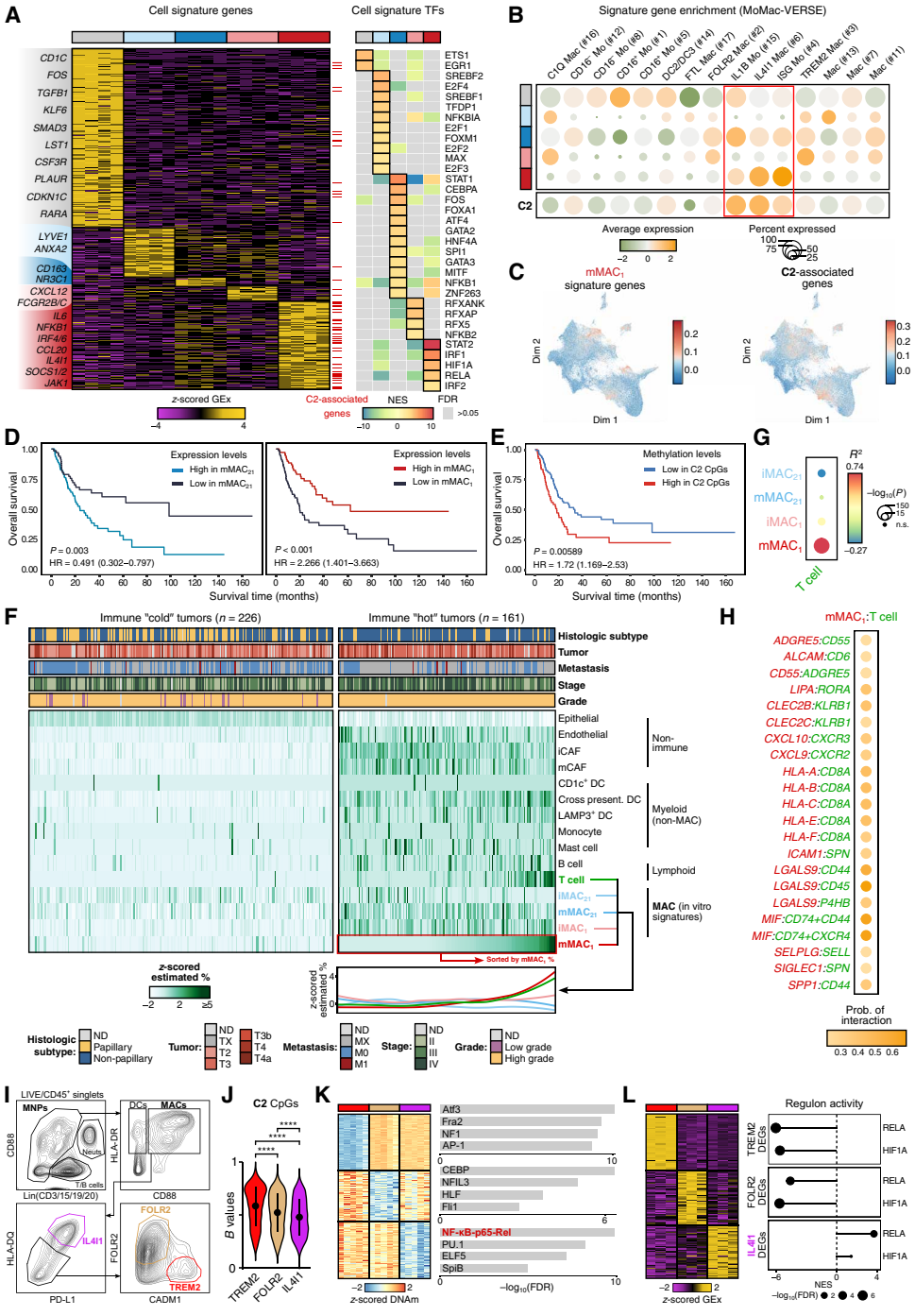

Fig. 5. Identification of MAC signatures on in vivo contexts. (**A**) Heatmap showing mRNA expression of signature DEGs specific to every experimental condition (MO, $iMAC_{21}$, $mMAC_{21}$, $iMAC_1$, and $mMAC_1$). (**B**) Dot plot showing the level of expression of the in vitro MAC-derived mRNA signatures along the C2-associated genes on the MoMac-VERSE. (**C**) UMAP with overlaid expression of $mMAC_1$ signature genes and C2-associated genes in the MoMac-VERSE. (**D**) Kaplan-Meier curves showing the association of MAC signatures with overall survival (OS) in bladder cancer [bladder urothelial carcinoma (BLCA)] patient samples (public data). (**E**) Kaplan-Meier curves showing association with C2 methylation profiles with OS in BLCA patient samples (public data). (**F**) Scaled cell type percentages in BLCA data. Heatmaps are separated by immune cold and hot tumors, characterized by low or high infiltration of immune cells, respectively. The clinical data associated with each patient are highlighted at the top. The LOESS curves show the distribution of MAC and T cell percentages at the bottom. (**G**) Correlation between MAC and T cell estimated percentages. (**H**) Significant interacting ligand-receptor pairs (red:green) between $mMAC_1$ and T cell, respectively, and the associated probability of interaction. (**I**) Representative flow cytometry plot of immune cells ($CD45^+$) in ovarian cancer, depicting the used sorting strategy for TREM2 (red), FOLR2 (orange), and IL4I1 (fuchsia) MAC populations. (**J**) Violin plots depicting unscaled B values of C2 cluster in TREM2, FOLR2, and IL4I1 ($n = 5$). (**K**) Heatmap of the demethylated regions specific to every sorted population (top 250 by FDR) and their associated TF motif enrichments (top 5), on the right. (**L**) Heatmap of the mRNA expression of signature DEGs specific to every population. The activity of the RELA and HIF1A regulons is shown on the right for every specific DEG set ($n = 3$). GEx, RNA expression; DNAm, DNA methylation. ****$P < 0.0001$.

A visual inspection of $mMAC_1$ signatures projected on the MoMac-VERSE uniform manifold approximation and projection (UMAP) is depicted in Fig. 5C. Figure S5B illustrates examples of MoMac-VERSE cluster-defining genes and their expression, both in the in vitro and the in vivo datasets. Last, to integrate all $mMAC_1$-associated molecular profiles (including mRNA expression, DNA methylation, and TF binding) in the in vivo context, we identified cells coexpressing any possible combination of these signatures and highlighted them in the MoMac-VERSE UMAP (fig. S5C). Again, IL1B Mo, IL4I1 Mac, and ISG Mo presented a relatively higher number of cells with the coexpression of $mMAC_1$ molecular signatures (in yellow), suggesting that these populations are the most similar in vivo equivalents to $mMAC_1$.

To determine the clinical relevance of MACs in human disease, we established the association between the presence of MAC population signatures (both in vitro and in vivo) and prognosis in cancer, as a model of in vivo–occurring hypoxia (*41*). Survival analysis on public human cancer data [The Cancer Genome Atlas (TCGA); see Supplementary Methods] determined that patients with high signatures/scores (i.e., a surrogate of high population infiltration in the tissue) of hypoxic MAC signatures ($iMAC_1$ and $mMAC_1$) generally displayed a better overall survival in several different cancer types (10 of 12 cases; fig. S5D). This association was also true for the IL4I1 MAC signature, which was associated with higher survival in 7 of 12 of the cancer types of the dataset, including bladder urothelial carcinoma (BLCA), ovarian carcinoma (OC), and others. Initially described as highly inflammatory cells with additional tolerogenic features (*10*), IL4I1-expressing MACs have recently been associated with good prognosis in colorectal cancer, where they are found within the tumor nests, performing active efferocytosis of cancer cells (*42*). In addition, in breast cancer, their presence predisposes to improved responses to immune checkpoint inhibitors, presumably owing to their high expression of immune checkpoint molecules (*42*).

In contrast, normoxic signatures ($iMAC_{21}$ and $mMAC_{21}$) were mainly associated with decreased survival (10 of 12). In line with this, the TREM2 MAC signature displayed the highest association with a poor prognosis, showing decreased survival in 7 of 12 cancer type series followed by FOLR2 MACs, with 6 of 12 (fig. S5D). In agreement with this, $TREM2^+$ MACs have been described as potent immunosuppressors in the TME and are usually found associated with progression and poor prognosis in a wide variety of cancers (*43*); FOLR2 is thought to be a marker of tissue-resident MACs (*44*), although its role in cancer is converse, tissue specific, and depends on additional polarization programs (*42*, *44*). Conversely, IL1B Mos were predominantly associated with decreased survival (in 5 of 12 cases), possibly because of the enrichment of this normoxic $mMAC_{21}$ transcriptomic signature in this population (Fig. 5B). In line with this, MACs expressing high amounts of IL-1β and displaying a mixed proinflammatory-immunosuppressive phenotype have been shown to correlate with poor prognosis in pancreatic ductal adenocarcinoma (*45*). $mMAC_1$ and IL4I1 signatures presented the highest overall concordance in terms of association with prognosis, presenting a matching effect in 6 of 12 cancer types.

Next, we focused on BLCA as a paradigm of cancer with the clearest separation in prognosis between $mMAC_1$ and $mMAC_{21}$. Kaplan-Meier curves (Fig. 5D and fig. S5E) illustrate MAC gene signatures associated with good ($mMAC_1$, IL4I1) or poor ($mMAC_{21}$, TREM2) prognosis. The DNA methylation status of BLCA tumors was also associated with prognosis; patients with low methylation levels in C2 CpGs displayed a significantly higher survival than patients with high methylation in the same regions (Fig. 5E).

To further elucidate the biological basis underlying the prognostic value of $mMAC_1$ in this cancer, we reanalyzed public scRNA-seq data of BLCA (*46*). In summary, we (i) annotated cells bearing the in vitro–derived MAC signatures, (ii) estimated the proportions of these cells, along with the rest of the populations, on BLCA tumor bulk RNA-seq data (TCGA) with CIBERSORTx, and (iii) revisited the scRNA-seq object to investigate cell-cell communication between populations of interest to characterize potential cellular mechanisms and interactions using CellChat (fig. S5F and Supplementary Methods). Estimation of cell population proportion in BLCA samples led to a first separation between immune "cold" and "hot" tumors, determined by a lower and higher immune/epithelial cell proportion ratio, respectively. These two groups were characterized by distinct clinical variables (e.g., tumor histology, size, metastasis, stage, and grade; Fig. 5F and Supplementary Methods). Immune hot tumors with a high estimated percentage of $mMAC_1$ also presented high percentages of other immune cell types, such as cross-presenting dendritic cells (DCs) and, most notably, T cells (Fig. 5F). In addition, these samples were largely devoid of non-immune cells (e.g., fibroblasts and endothelial cells) and normoxic MACs ($iMAC_{21}$ and $mMAC_{21}$). Of note, T cell percentage was significantly correlated with $mMAC_1$ ($r = 0.74$, $P = 2.2{\cdot}10^{-67}$) and, opposingly, anticorrelated with $iMAC_{21}$ ($r = -0.27$, $P = 5{\cdot}10^{-8}$) along all the patient series [Fig. 5, G and F (bottom)].

Cell-cell communication analysis revealed several significant ligand-receptor pairs between $mMAC_1$ and T cells, related to T cell chemotaxis (*CXCL9:CXCR3* and *CXCL10:CXCR2*) and trafficking (*ICAM1:SPN*), as well as T cell receptor (TCR) activation through MHC class I (*HLA-A/B/C/E/F:CD8*) and additional costimulatory interactions (*MIF:CD74* + *CD44/CXCR4*), among others (Fig. 5H). In summary, this analysis suggests that $mMAC_1$ display enhanced T cell–activating features, potentially contributing to an increased immunogenic status of the TME in BLCA tumors, leading to improved outcomes of these patients.

Last, we isolated these MAC populations from primary ovarian tumors. We used OC samples for practical reasons, such as the inherently large weight of these tumors, which are characterized by a substantial MAC infiltration and a marked hypoxia (*47*, *48*). Of note, OC also showed a clean separation between the normoxic ($mMAC_{21}$) and hypoxic ($mMAC_1$) populations with regard to prognosis in our previous analysis (fig. S5D). Through sorting by flow cytometry, we purified IL4I1, TREM2, and FOLR2 MACs through a gating strategy developed in (*10*) with additional optimizations (Fig. 5I and Supplementary Methods). The expression of marker genes (defined in the MoMac-VERSE) was confirmed in every population by bulk RNA-seq (fig. S5G), supporting the validity of the sorting strategy. DNA methylation profiling revealed a general recapitulation of the methylation dynamics of C2, in which the IL4I1 population showed the lowest average methylation levels (Fig. 5J). p65 was the most enriched motif in the demethylated CpGs associated specifically with IL4I1 (Fig. 5K). When comparing each population against the rest, the expression of genes in the RELA and HIF1A regulons were only up-regulated in IL4I1, whereas they were found relatively down-regulated in TREM2 and FOLR2 (Fig. 5L). Additional regulons such as RFX5, NFKB1, IRF1, and E2F4, among others, were found among the top associated with

both IL4I1 (fig. S5H) and $mMAC_I$ (Fig. 2F), reinforcing the similarity between these two cellular programs.

In summary, we conclude that the in vitro properties of $mMAC_I$ are displayed by in vivo MAC populations present in human cancer samples such as IL4I1 MACs, including the demethylation and upregulation of NF-κB–associated genes, as well as hypoxic and additional inflammatory signatures.

DISCUSSION

In this work, we demonstrate that hypoxia enhances the acquisition of immunogenic features during MAC activation. Underlying this hyperimmunogenic boosting, we identify a group of proinflammatory genes that undergo DNA demethylation and overexpression in hypoxic conditions. Despite the implication of both HIF1α and NF-κB in the vast transcriptional reprogramming associated with hypoxia, the p65 subunit of NF-κB is the primary driver of the DNA demethylation process, associated with the activation of critical inflammatory cytokines such as IL-6 and TNF-α. These molecular features are found in vivo and enriched in tissue MAC populations in pathogenic contexts such as cancer. In that setting, hypoxic inflammatory signatures (both their in vitro and in vivo homologs) are associated with better survival in a range of human cancers with immune infiltration, including bladder and ovarian carcinomas. We propose that changes in the cellular cross-talk between inflammatory hypoxic MACs and T cell populations are responsible for the improved immune response in these tumors.

TET-mediated DNA methylation changes are crucial for myeloid cell function in vitro and in vivo (*49*, *50*). The enzymatic activity of TET methylcytosine dioxygenases depends on several cofactors, including Fe^{2+}, α-ketoglutarate, and oxygen (*51*). In this line, previous studies have shown that tumor hypoxia causes DNA hypermethylation by reducing TET activity (*26*). In our study, we observed that limited oxygen availability also results in an inhibition of demethylation for a large cluster of CpGs that demethylate during normal MAC differentiation. However, unexpectedly, even under TET-inhibitory conditions such as 1% oxygen, there is a significant de novo DNA demethylation of proinflammatory genes controlled by NF-κB, specific to hypoxic conditions. This highlights a paradoxical mechanism where NF-κB is able to override the effect of hypoxia and enhances TET-mediated demethylation for a specific group of proinflammatory genes. Of note, to interrogate the gene regulatory role of DNA methylation, further time-resolved analyses of paired methylome and transcriptome would be required to establish the sequence of events.

The proposed effects of hypoxia and HIFs on MAC function are highly contradictory, with examples demonstrating their influence on both immunogenic- and immunosuppressive-promoting capacities (*15*, *38*, *52*, *53*). Our study supports that hypoxia can promote immunogenic properties in MACs, characterized by increased inflammatory cytokine secretion and surface marker expression, and, most importantly, by a loss in the T cell–suppressive capacity, characteristic of M-CSF MO-derived MACs (*54*). At the transcriptional level, MACs activated in hypoxia displayed not only increased hypoxic and glycolytic signatures but also additional immune-related signaling pathways, including IFN, TNF, STAT, and NF-κB, when compared with their normoxic counterparts. Of note, hypoxia-associated DNA demethylation was mainly associated with a transcriptional boosting of LPS-response genes, consisting of NF-κB targets that already up-regulate in normoxic LPS but whose levels markedly increase when LPS is administered in hypoxia. Activation in hypoxia was sufficient to achieve the transcriptional boosting of these genes, highlighting the importance of the coexistence of both stimuli for the acquisition of the phenotype. Nevertheless, some features induced by hypoxia (i.e., loss of $CD8^+$ T cell suppression) were indeed perdurable after cellular reoxygenation, suggesting the existence of additional phenotypical rewiring that is independent of activation in hypoxic conditions.

Of note, it is critical to acknowledge that MAC polarization in vivo is produced in response to complex cues in the microenvironment, leading to a functionally diversified myriad of populations. Hence, even if, in our case, the joint effect of hypoxia plus an immunogenic stimulus (i.e., LPS) leads to the increase of immunogenic features, we do not discard that, in the presence of, for instance, an anti-inflammatory signal (e.g., IL-10 and transforming growth factor–β), the resulting consequence upon the MAC state is different or inverse (e.g., boosting of immunosuppressive features) (*55*). A limitation of this study is the use of one stimulus at a time (LPS or other PAMPs, TNF-α, or IL-1β), which possibly does not account for the complexity found in physiological contexts. However, contrary to in vivo experiments, where ascertaining the effect and contribution of multiple signals is more complicated, we believe that our model is clear in showing that the isolated effect of hypoxia plus an additional inflammatory ligand reproducibly induces an inflammatory-boosting effect.

Inspection of the binding profiles of HIF1α and p65, the two most significantly enriched TFs in our analyses of the methylomics and transcriptomics data, revealed a set of genes that are commonly bound by both proteins around the same regions. Despite showing HIF1α-driven profiles, genes bound by both HIF1α and p65 were mostly associated with immune-related functions, reinforcing the role of HIF1α as a regulator of immunity and inflammation, aside from its role in hypoxia (*56*, *57*). The expression of commonly bound genes was activated by any of the two independent stimuli (hypoxia or LPS), suggesting a mechanistic convergence in the response to these two signals, which deserves further investigation. However, the specific demethylation in hypoxia was exclusively dependent on p65, suggesting the involvement of HIF-independent hypoxic p65 overactivation mechanisms (*58*). All of this implies the concurrence of several independent mechanisms underlying the hypoxic inflammatory boosting, highlighting this phenomenon as a biologically relevant process.

Hypoxia in the TME has been classically linked with the acquisition of detrimental features in MACs (*55*), where their presence is found widely associated with worse patient prognosis or response to treatment (*59*, *60*). However, these studies often regard MACs as a whole, overlooking their ontogeny, heterogeneity, or localization within the tumor, and also fail to determine molecular signals driving specific subpopulations of these inherently plastic cells (*61*, *62*). In this study, when we inspected human cancer data, patients bearing a high hypoxic inflammatory signature (or of their in vivo equivalent population), showed, in general, a higher overall survival, suggesting a protective role of these cells. It should be noted that this relationship between MAC abundance and clinical outcome was highly context specific, with associations in opposite trends depending on the cancer type. This is in line with previous findings suggesting that one given MAC population may have opposing roles in different cancers (*63*).

When focusing on examples where hypoxic inflammatory MACs were of prognostic value, such as BLCA, we identified that the abundance of these cells significantly correlated with tumors that are heavily infiltrated by T cells. Predictive analyses on BLCA scRNA-seq data suggested significant interactions between these two cell types, pointing to increased chemotaxis and activation of T cells through antigen cross-presentation by MHC class I. This function, classically associated with DCs, has also been described in human in vivo MO-derived MACs in cancer ascites (*64*). Together, these results suggest that hypoxia prompts the activation of several mechanisms in activated MACs that boost not only their own inflammatory features but also their ability to activate other immune cells.

Collectively, our study revealed that, in isolated inflammatory conditions, hypoxia has a net effect of boosting the immunogenic properties of MACs. We propose a model in which, under conditions that inhibit DNA demethylation due to limited access to oxygen, NF-κB–mediated activation overcomes this inhibitory trend and achieves increased demethylation of a cluster of inflammatory genes, provoking their overexpression. This leads to the acquisition of immunological and molecular signatures that are associated with good prognosis in human cancers, in a process that is regulated by TET2 and the TFs NF-κB and HIF1α. This poses specific hypoxic inflammatory MAC populations as promising actionable targets to modulate responses to cancer and underpins DNA methylation as a potential manipulable mechanism to fine-tune MAC states.

MATERIALS AND METHODS

Study design

This study was designed to characterize the effect of hypoxia on MAC differentiation and activation. As an experimental system, we used human MO-derived MACs, in which we interrogated the epigenetic (DNA methylation), transcriptional (RNA-seq), TF binding (ChIP-seq), and protein expression (flow cytometry) profiles in normoxia and hypoxia, in steady state, and under several stimuli. Through our research, we identified an in vivo MAC subpopulation exhibiting features consistent with our observations. To confirm our findings, we isolated these MACs from ovarian cancer samples and assessed their DNA methylation and transcriptional profiles. Replicates in all figures refer to independent biological replicates, and the statistical tests used in each analysis are detailed in the corresponding figure legend.

Obtention of healthy human buffy coats

Healthy, anonymous donor-derived buffy coats were obtained through the Catalan Blood and Tissue Bank (CBTB), following the principles of the World Medical Association Declaration of Helsinki. Before providing the first blood sample, all donors received detailed oral and written information and signed a consent form at the CBTB. The study was approved by the board of the Bellvitge Hospital Ethical Committee (PR275/17).

Monocyte purification and MAC differentiation in vitro

Peripheral blood mononuclear cells (PBMCs) were isolated by Ficoll-Paque gradient centrifugation. Monocytes were isolated from PBMCs using positive selection with MACS magnetic bead–coupled CD14 antibody (Miltenyi, 130-050-201).

To obtain differentiated MACs, purified MOs were cultured in RPMI 1640 + GlutaMAX (Gibco, Thermo Fisher Scientific) containing 10% of heat-inactivated fetal bovine serum (FBS), penicillin (100 U/ml), streptomycin (100 μg/ml), and human M-CSF (15 ng/ml; PeproTech). Immediately after the addition of M-CSF, MAC plates were placed in a normoxic (21% O_2) or hypoxic (1% O_2) CO_2 incubator at 37°C, 5% CO_2, and 80 to 90% humidity for 5 days. At day 5, MACs were stimulated with LPS (10 ng/ml; Sigma-Aldrich) or an equivalent volume of phosphate-buffered saline (PBS) for 2 to 48 hours, depending on the experiment. The hypoxic workstation (Whitley H35 Hypoxystation, Don Whitley Scientific, UK) was calibrated less than 2 weeks before all experiments.

When indicated, $iMAC_{21}$ and $iMAC_1$ at day 5 were stimulated for 48 hours with the following ligands at different final concentrations: P3C (10 μg/ml; IBIAN Technologies, S.L.), CpG (3 μg/ml; ODN 2006, InvivoGen), poly(I:C) (10 μg/ml; InvivoGen), human TNF-α (10 ng/ml; PeproTech), or IL-1β (10 ng/ml; PeproTech).

Quantification of cytokines in cell culture supernatants

IL-6, TNF-α, and IL-10 proteins were quantified in cell culture supernatants at the end of the MAC differentiation protocol (day 7) with the LEGENDplex Human Inflammation Panel 1 (BioLegend), following the manufacturer's instructions.

Flow cytometry of cultured cells

The expression of extracellular surface protein expression was assessed by flow cytometry. To detach cells, culture medium was removed and substituted with cold fluorescence-activated cell sorting (FACS) buffer (PBS containing 4% FBS and 2 mM EDTA). After 5 min, cells were gently detached with rubber-capped cell scrapers (Sarstedt). Nonspecific antibody binding was blocked by incubating cells with anti-CD16/CD32 antibody for 5 min at 4°C. Then, 10^5 cells per condition were incubated in FACS buffer for 20 min at 4°C in the dark with optimal concentration of the following fluorophore-conjugated antibodies: HLA-DR-PE/Cy7 (BioLegend, clone L246), CD86-APC (Miltenyi, clone FM95), CD80-PE (Miltenyi, clone 2D10), CD14-APC (Miltenyi, clone TÜK4), CD206-PE/Cy7 (BioLegend, clone 15-2), and CD163-FITC (BioLegend, clone GHI/61). Stained cells were analyzed on a FACSCanto II (BD Biosciences). FlowJo v10.9.0 (FlowJo LLC) was used to export fluorescence data and generate histogram plots.

Cytotoxic T cell proliferation assay

Allogenic cytotoxic ($CD8^+$) T cells were isolated by negative selection using Dynabeads Untouched Human CD8 T Cells Kit (Invitrogen) and labeled with carboxyfluorescein succinimidyl ester (CFSE) CellTrace (Invitrogen), in accordance with the manufacturer's instructions.

Purified $CD8^+$ T cells were seeded in round-bottom 96-well plates (2×10^5 cells per well), and MACs were added at a ratio of 1:3 (approximately 65,000 cells per well). To stimulate $CD8^+$ T cell proliferation, 5 μl of anti-CD3/CD28 Dynabeads (Invitrogen) were added to each well, except in negative controls, and additional complete medium was added in every well until a total volume of 200 μl was reached. After 4 days, $CD8^+$ T cell proliferation was analyzed by FACS and determined by estimating the percentage of cells with decreased CFSE staining compared to unstimulated $CD8^+$ T cells.

Real-time quantitative reverse transcription polymerase chain reaction

Total RNA was extracted with using a Maxwell RSC simplyRNA Cells Kit (Promega) and subjected to reverse transcription with the

Transcriptor First Strand cDNA Synthesis Kit (Roche) following the manufacturer's instructions. Real-time quantitative reverse transcription polymerase chain reaction (qRT-PCR) was performed in three technical replicates per sample using LightCycler 480 SYBR Green Mix (Roche) using 5 ng of cDNA per replicate. The ΔΔCt method was used to determine the relative expression of target genes, and *RPL38* was used as a housekeeping gene. qRT-PCR primers for the selected genes are described in table S3.

Western blotting

After removing the medium and washing with PBS, whole-cell protein lysates were obtained by adding Laemmli buffer (LB; 5× SDS-PAGE Sample Loading Buffer, NZYtech) directly to cell culture plates (200 μl of LB per 15×10^6 cells) at the indicated time points. Lysates were then sonicated and loaded, and proteins were separated by SDS–polyacrylamide gel electrophoresis. Resolved proteins were transferred to polyvinylidene difluoride membranes, and immunoblotting was performed as described in (*65*). Primary antibodies were used at the following concentrations: 1:1000 anti-HIF1α (Novus Biologicals, NB100-134), 1:1000 anti-p65 (Diagenode, 615310256), and 1:100 anti–α-tubulin (Rockland Immunochemicals, 200-301-880).

Immunofluorescence

Cells were fixed with PBS + 4% paraformaldehyde for 20 min and then washed two times with PBS. Fixed cells were permeabilized with PBS + Triton X-100 (0.5%) for 10 min at room temperature. Coverslips were washed twice with PBS and blocked with PBS + 4% bovine serum albumin (BSA) for 1 hour at room temperature. Anti-human HIF1α (Novus Biologicals, NB100-134) or anti-human p65 (Abcam, ab16502), both at 1:200 with PBS + 4% BSA, were incubated overnight. Then, cells were washed four times for 15 min at room temperature with PBS and incubated with anti-rabbit Alexa Fluor 488 (1:300; Invitrogen, A-11008) for 1 hour in PBS + 4% BSA. Then, preparations were washed four times for 15 min at room temperature with PBS and incubated with 1:500 Phalloidin Alexa Fluor 568 (Invitrogen, A12380) for 30 min in the dark. Preparations were washed three times for 5 min with PBS and stained with 4′,6-diamidino-2-phenylindole (2 μg/ml). VECTASHIELD (Vector Laboratories) was used as a mounting medium. Images were taken with Leica STELLARIS 8.

Human ovarian tumor samples

Tumor tissue from ovaries was obtained from patients with high-grade serous ovarian carcinoma ($n = 5$) following written informed consent (Gustave Roussy Hospital, Villejuif, France) and ethical approval (N°ID-RCB: 2015-A01183-46).

Tissue processing

Tissues were transferred to a sterile tissue culture dish and cut into small fragments (1 to 2 mm) with scissors and incubated with digestion buffer [collagenase IV (0.2 mg/ml; Sigma-Aldrich, C5138-500MG] and deoxyribonuclease IU (20,000 IU/ml; Roche, 11284932001) dissolved in RPMI + 10% FBS) for 30 to 40 min at 37°C. Digested tissue was then mechanically disaggregated by resuspension using a 3-ml syringe with a 18-gauge needle, filtered through a 70-μm strainer (Starlab, CC8111-0072), and centrifuged at 400*g* for 8 min at 4°C. When needed, pellets were then resuspended in 5 ml of RBC lysis buffer (eBioscience, 00-4333-57), incubated on ice for 5 to 10 min, and washed with additional RPMI. Last, cells were counted, centrifuged, and resuspended in CryoStor CS10 (STEMCELL, 100-1061) at a concentration of 1×10^6 to 20×10^6 cells/ml before cryopreservation.

Cell sorting of tumor-associated MACs

Cryopreserved cells were thawed in a water bath at 37°C and instantly diluted with prewarmed RPMI + 10% FBS. Cells were washed and incubated with Live/Dead blue dye (Invitrogen) for 20 min at 4°C in PBS and then resuspended and blocked in PBS + 20% FBS for 15 min at 4°C. Then, cells were incubated in FACS buffer for 30 min at 4°C with the appropriate volumes of the following primary antibodies: CD45-PerCP (BioLegend, clone 2D1), CD3-BV650 (BioLegend, clone UCHT1), CD19-BV650 (BioLegend, clone HIB19), CD20-BV650 (BioLegend, clone 2H7), CD15-BV650 (BioLegend, clone SSEA-1), CD16-APC-Cy7 (BioLegend, clone 3G8), HLA-DR–Alexa Fluor 700 (BioLegend, clone LN3), HLA-DQ–BV510 (BD, clone Tu169), CD14-BUV737 (BD, clone M5E2), CD88-FITC (BioLegend, clone S5/1), PD-L1–Alexa Fluor 594 (BioLegend, clone 29E.2A3), FOLR2-PE (BioLegend, clone 94b.FOLR2), CD206-BUV395 (BD, clone 19.2), CD207-PE-Vio770 (Miltenyi, clone MB22-9F5), CD141-BV421 (BioLegend, clone M80), CD1c-BV785 (BioLegend, clone L161), and chicken anti-human CADM1 IgY primary antibody (MBL, clone 3E1). Cells were washed and incubated with secondary antibody anti-chicken–Alexa Fluor 647 for 20 additional minutes at 4°C. Cells were then washed with FACS buffer, resuspended in RPMI + 10% FBS, and passed through a 40-μm strainer (Starlab, CC8111-0042). Last, cells were sorted in a FACSAria Fusion (BD Biosciences) at a purity of <95%.

Statistical analysis

Statistical tests used in every figure are specified on their respective figure legends. As a general rule: Bar plots represent means ± SEM; box plots represent the median and interquartile range (IQR), and lines outside the boxes represent the 25th percentile minus 1.5 times the IQR and the 75th percentile plus 1.5 times the IQR. Violin plots depict data distribution density curves. Significance values were computed with functions from R's stats package unless specified otherwise. *P* values were adjusted by the FDR method when indicated. Significance values were summarized as follows: $*P < 0.05$, $**P < 0.01$, $***P < 0.001$, and $****P < 0.0001$.

Supplementary Materials

The PDF file includes:

Supplementary Methods
Figs. S1 to S5
Legends for tables S1 to S5
References

Other Supplementary Material for this manuscript includes the following:

Tables S1 to S5

REFERENCES AND NOTES

1. C. Blériot, S. Chakarov, F. Ginhoux, Determinants of resident tissue macrophage identity and function. *Immunity* **52**, 957–970 (2020).
2. M. D. Park, A. Silvin, F. Ginhoux, M. Merad, Macrophages in health and disease. *Cell* **185**, 4259–4279 (2022).
3. E. Mass, F. Nimmerjahn, K. Kierdorf, A. Schlitzer, Tissue-specific macrophages: How they develop and choreograph tissue biology. *Nat. Rev. Immunol.* **23**, 563–579 (2023).
4. M. Guilliams, G. R. Thierry, J. Bonnardel, M. Bajenoff, Establishment and maintenance of the macrophage niche. *Immunity* **52**, 434–451 (2020).

5. Y. Lavin, A. Mortha, A. Rahman, M. Merad, Regulation of macrophage development and function in peripheral tissues. *Nat. Rev. Immunol.* **15**, 731–744 (2015).
6. Y. Okabe, R. Medzhitov, Tissue biology perspective on macrophages. *Nat. Immunol.* **17**, 9–17 (2016).
7. J. Xue, S. V. Schmidt, J. Sander, A. Draffehn, W. Krebs, I. Quester, D. de Nardo, T. D. Gohel, M. Emde, L. Schmidleithner, H. Ganesan, A. Nino-Castro, M. R. Mallmann, L. Labzin, H. Theis, M. Kraut, M. Beyer, E. Latz, T. C. Freeman, T. Ulas, J. L. Schultze, Transcriptome-based network analysis reveals a spectrum model of human macrophage activation. *Immunity* **40**, 274–288 (2014).
8. Y. Lavin, D. Winter, R. Blecher-Gonen, E. David, H. Keren-Shaul, M. Merad, S. Jung, I. Amit, Tissue-resident macrophage enhancer landscapes are shaped by the local microenvironment. *Cell* **159**, 1312–1326 (2014).
9. D. Gosselin, V. M. Link, C. E. Romanoski, G. J. Fonseca, D. Z. Eichenfield, N. J. Spann, J. D. Stender, H. B. Chun, H. Garner, F. Geissmann, C. K. Glass, Environment drives selection and function of enhancers controlling tissue-specific macrophage identities. *Cell* **159**, 1327–1340 (2014).
10. K. Mulder, A. A. Patel, W. T. Kong, C. Piot, E. Halitzki, G. Dunsmore, S. Khalilnezhad, S. E. Irac, A. Dubuisson, M. Chevrier, X. M. Zhang, J. K. C. Tam, T. K. H. Lim, R. M. M. Wong, R. Pai, A. I. S. Khalil, P. K. H. Chow, S. Z. Wu, G. Al-Eryani, D. Roden, A. Swarbrick, J. K. Y. Chan, S. Albani, L. Derosa, L. Zitvogel, A. Sharma, J. Chen, A. Silvin, A. Bertoletti, C. Blériot, C.-A. Dutertre, F. Ginhoux, Cross-tissue single-cell landscape of human monocytes and macrophages in health and disease. *Immunity* **54**, 1883–1900.e5 (2021).
11. P. Vaupel, F. Kallinowski, P. Okunieff, Blood flow, oxygen and nutrient supply, and metabolic microenvironment of human tumors: A review. *Cancer Res.* **49**, 6449–6465 (1989).
12. C. R. Stevens, R. B. Williams, A. J. Farrell, D. R. Blake, Hypoxia and inflammatory synovitis: Observations and speculation. *Ann. Rheum. Dis.* **50**, 124–132 (1991).
13. J. Kivisaari, Oxygen and carbon dioxide tensions in healing tissue. *Acta Chir. Scand.* **141**, 693–696 (1975).
14. A. Palazon, A. W. Goldrath, V. Nizet, R. S. Johnson, HIF transcription factors, inflammation, and immunity. *Immunity* **41**, 518–528 (2014).
15. T. Cramer, Y. Yamanishi, B. E. Clausen, I. Förster, R. Pawlinski, N. Mackman, V. H. Haase, R. Jaenisch, M. Corr, V. Nizet, G. S. Firestein, H. P. Gerber, N. Ferrara, R. S. Johnson, HIF-1α is essential for myeloid cell-mediated inflammation. *Cell* **112**, 645–657 (2003).
16. C. A. Corzo, T. Condamine, L. Lu, M. J. Cotter, J.-I. Youn, P. Cheng, H.-I. Cho, E. Celis, D. G. Quiceno, T. Padhya, T. V. McCaffrey, J. C. McCaffrey, D. I. Gabrilovich, HIF-1α regulates function and differentiation of myeloid-derived suppressor cells in the tumor microenvironment. *J. Exp. Med.* **207**, 2439–2453 (2010).
17. I. B. Barsoum, C. A. Smallwood, D. R. Siemens, C. H. Graham, A mechanism of hypoxia-mediated escape from adaptive immunity in cancer cells. *Cancer Res.* **74**, 665–674 (2014).
18. Y. Gropper, T. Feferman, T. Shalit, T.-M. Salame, Z. Porat, G. Shakhar, Culturing CTLs under hypoxic conditions enhances their cytolysis and improves their anti-tumor function. *Cell Rep.* **20**, 2547–2555 (2017).
19. J. L. Platt, R. Salama, J. Smythies, H. Choudhry, J. O. Davies, J. R. Hughes, P. J. Ratcliffe, D. R. Mole, Capture-C reveals preformed chromatin interactions between HIF-binding sites and distant promoters. *EMBO Rep.* **17**, 1410–1421 (2016).
20. M. Batie, J. Frost, D. Shakir, S. Rocha, Regulation of chromatin accessibility by hypoxia and HIF. *Biochem. J.* **479**, 767–786 (2022).
21. M. Tausendschön, N. Dehne, B. Brüne, Hypoxia causes epigenetic gene regulation in macrophages by attenuating Jumonji histone demethylase activity. *Cytokine* **53**, 256–262 (2011).
22. A. Garcia-Gomez, T. Li, M. Kerick, F. Català-Moll, N. R. Comet, J. Rodríguez-Ubreva, L. Rica, M. R. Branco, J. Martín, E. Ballestar, TET2- and TDG-mediated changes are required for the acquisition of distinct histone modifications in divergent terminal differentiation of myeloid cells. *Nucleic Acids Res.* **45**, 10002–10017 (2017).
23. T. Li, A. Garcia-Gomez, O. Morante-Palacios, L. Ciudad, S. Özkaramehmet, E. Van Dijck, J. Rodríguez-Ubreva, A. Vaquero, E. Ballestar, SIRT1/2 orchestrate acquisition of DNA methylation and loss of histone H3 activating marks to prevent premature activation of inflammatory genes in macrophages. *Nucleic Acids Res.* **48**, 665–681 (2020).
24. S. Ito, A. C. D'Alessio, O. V. Taranova, K. Hong, L. C. Sowers, Y. Zhang, Role of Tet proteins in 5mC to 5hmC conversion, ES-cell self-renewal and inner cell mass specification. *Nature* **466**, 1129–1133 (2010).
25. K. Joshi, S. Liu, P. Breslin SJ, J. Zhang, Mechanisms that regulate the activities of TET proteins. *Cell. Mol. Life Sci.* **79**, 363 (2022).
26. B. Thienpont, J. Steinbacher, H. Zhao, F. D'Anna, A. Kuchnio, A. Ploumakis, B. Ghesquière, L. Van Dyck, B. Boeckx, L. Schoonjans, E. Hermans, F. Amant, V. N. Kristensen, K. Peng Koh, M. Mazzone, M. Coleman, T. Carell, P. Carmeliet, D. Lambrechts, Tumour hypoxia causes DNA hypermethylation by reducing TET activity. *Nature* **537**, 63–68 (2016).
27. J. A. Smythies, M. Sun, N. Masson, R. Salama, P. D. Simpson, E. Murray, V. Neumann, M. E. Cockman, H. Choudhry, P. J. Ratcliffe, D. R. Mole, Inherent DNA-binding specificities of the HIF-1α and HIF-2α transcription factors in chromatin. *EMBO Rep.* **20**, e46401 (2019).
28. F. D'Anna, L. Van Dyck, J. Xiong, H. Zhao, R. V. Berrens, J. Qian, P. Bieniasz-Krzywiec, V. Chandra, L. Schoonjans, J. Matthews, J. De Smedt, L. Minnoye, R. Amorim, S. Khorasanizadeh, Q. Yu, L. Zhao, M. De Borre, S. N. Savvides, M. C. Simon, P. Carmeliet, W. Reik, F. Rastinejad, M. Mazzone, B. Thienpont, D. Lambrechts, DNA methylation repels binding of hypoxia-inducible transcription factors to maintain tumor immunotolerance. *Genome Biol.* **21**, 182 (2020).
29. I. B. Barsoum, T. K. Hamilton, X. Li, T. Cotechini, E. A. Miles, D. R. Siemens, C. H. Graham, Hypoxia induces escape from innate immunity in cancer cells via increased expression of ADAM10: Role of nitric oxide. *Cancer Res.* **71**, 7433–7441 (2011).
30. P. Jayaprakash, M. Ai, A. Liu, P. Budhani, T. Bartkowiak, J. Sheng, C. Ager, C. Nicholas, A. R. Jaiswal, Y. Sun, K. Shah, S. Balasubramanyam, N. Li, G. Wang, J. Ning, A. Zal, T. Zal, M. A. Curran, Targeted hypoxia reduction restores T cell infiltration and sensitizes prostate cancer to immunotherapy. *J. Clin. Invest.* **128**, 5137–5149 (2018).
31. L. de la Rica, J. Rodríguez-Ubreva, M. García, A. B. M. M. K. Islam, J. M. Urquiza, H. Hernando, J. Christensen, K. Helin, C. Gómez-Vaquero, E. Ballestar, PU.1 target genes undergo Tet2-coupled demethylation and DNMT3b-mediated methylation in monocyte-to-osteoclast differentiation. *Genome Biol.* **14**, R99 (2013).
32. J. M. Müller, H. W. Ziegler-Heitbrock, P. A. Baeuerle, Nuclear factor kappa B, a mediator of lipopolysaccharide effects. *Immunobiology* **187**, 233–256 (1993).
33. M. U. Kaikkonen, N. J. Spann, S. Heinz, C. E. Romanoski, K. A. Allison, J. D. Stender, H. B. Chun, D. F. Tough, R. K. Prinjha, C. Benner, C. K. Glass, Remodeling of the enhancer landscape during macrophage activation is coupled to enhancer transcription. *Mol. Cell* **51**, 310–325 (2013).
34. J. Ernst, M. Kellis, ChromHMM: Automating chromatin-state discovery and characterization. *Nat. Methods* **9**, 215–216 (2012).
35. M. J. Ziller, H. Gu, F. Müller, J. Donaghey, L. T.-Y. Tsai, O. Kohlbacher, P. L. De Jager, E. D. Rosen, D. A. Bennett, B. E. Bernstein, A. Gnirke, A. Meissner, Charting a dynamic DNA methylation landscape of the human genome. *Nature* **500**, 477–481 (2013).
36. L. Garcia-Alonso, C. H. Holland, M. M. Ibrahim, D. Turei, J. Saez-Rodriguez, Benchmark and integration of resources for the estimation of human transcription factor activities. *Genome Res.* **29**, 1363–1375 (2019).
37. M. Simón-Fuentes, C. Herrero, L. Acero-Riaguas, C. Nieto, F. Lasala, N. Labiod, J. Luczkowiak, B. Alonso, R. Delgado, M. Colmenares, Á. L. Corbí, Á. Domínguez-Soto, TLR7 activation in M-CSF-dependent monocyte-derived human macrophages potentiates inflammatory responses and prompts neutrophil recruitment. *J. Innate Immun.* **15**, 517–530 (2023).
38. E. Izquierdo, V. D. Cuevas, S. Fernández-Arroyo, M. Riera-Borrull, E. Orta-Zavalza, J. Joven, E. Rial, A. L. Corbi, M. M. Escribese, Reshaping of human macrophage polarization through modulation of glucose catabolic pathways. *J. Immunol.* **195**, 2442–2451 (2015).
39. R. Abou Khouzam, R. F. Zaarour, K. Brodaczewska, B. Azakir, G. H. Venkatesh, J. Thiery, S. Terry, S. Chouaib, The effect of hypoxia and hypoxia-associated pathways in the regulation of antitumor response: Friends or foes? *Front. Immunol.* **13**, 828875 (2022).
40. L.-L. Chen, C. Morcelle, Z.-L. Cheng, X. Chen, Y. Xu, Y. Gao, J. Song, Z. Li, M. D. Smith, M. Shi, Y. Zhu, N. Zhou, M. Cheng, C. He, K.-Y. Liu, G. Lu, L. Zhang, C. Zhang, J. Zhang, Y. Sun, T. Qi, Y. Lyu, Z.-Z. Ren, X.-M. Tan, J. Yin, F. Lan, Y. Liu, H. Yang, M. Qian, C. Duan, X. Chang, Y. Zhou, L. Shen, A. S. Baldwin, K.-L. Guan, Y. Xiong, D. Ye, Itaconate inhibits TET DNA dioxygenases to dampen inflammatory responses. *Nat. Cell Biol.* **24**, 353–363 (2022).
41. M. Höckel, P. Vaupel, Tumor hypoxia: Definitions and current clinical, biologic, and molecular aspects. *J. Natl. Cancer Inst.* **93**, 266–276 (2001).
42. M. Matusiak, J. W. Hickey, D. G. P. van IJzendoorn, G. Lu, L. Kidzinski, S. Zhu, D. R. C. Colburg, B. Luca, D. J. Phillips, S. W. Brubaker, G. W. Charville, J. Shen, K. M. Loh, D. K. Okwan-Duodu, G. P. Nolan, A. M. Newman, R. B. West, M. van de Rijn, Spatially segregated macrophage populations predict distinct outcomes in colon cancer. *Cancer Discov.* **14**, 1418–1439 (2024).
43. M. Molgora, E. Esaulova, W. Vermi, J. Hou, Y. Chen, J. Luo, S. Brioschi, M. Bugatti, A. S. Omodei, B. Ricci, C. Fronick, S. K. Panda, Y. Takeuchi, M. M. Gubin, R. Faccio, M. Cella, S. Gilfillan, E. R. Unanue, M. N. Artyomov, R. D. Schreiber, M. Colonna, TREM2 modulation remodels the tumor myeloid landscape enhancing anti-PD-1 immunotherapy. *Cell* **182**, 886–900.e17 (2020).
44. R. N. Ramos, Y. Missolo-Koussou, Y. Gerber-Ferder, C. P. Bromley, M. Bugatti, N. G. Núñez, J. T. Boari, W. Richer, L. Menger, J. Denizeau, C. Sedlik, P. Caudana, F. Kotsias, L. L. Niborski, S. Viel, M. Bohec, S. Lameiras, S. Baulande, L. Lesage, A. Nicolas, D. Meseure, A. Vincent-Salomon, F. Reyal, C.-A. Dutertre, F. Ginhoux, L. Vimeux, E. Donnadieu, B. Buttard, J. Galon, S. Zelenay, W. Vermi, P. Guermonprez, E. Piaggio, J. Helft, Tissue-resident FOLR2$^+$ macrophages associate with CD8$^+$ T cell infiltration in human breast cancer. *Cell* **185**, 1189–1207.e25 (2022).
45. N. Caronni, F. La Terza, F. M. Vittoria, G. Barbiera, L. Mezzanzanica, V. Cuzzola, S. Barresi, M. Pellegatta, P. Canevazzi, G. Dunsmore, C. Leonardi, E. Montaldo, E. Lusito, E. Dugnani, A. Citro, M. S. F. Ng, M. S. Lena, D. Drago, A. Andolfo, S. Brugiapaglia, A. Scagliotti, A. Mortellaro, V. Corbo, Z. Liu, A. Mondino, P. Dellabona, L. Piemonti, C. Taveggia, C. Doglioni, P. Cappello, F. Novelli, M. Iannacone, L. G. Ng, F. Ginhoux, S. Crippa, M. Falconi,

C. Bonini, L. Naldini, M. Genua, R. Ostuni, IL-1β+ macrophages fuel pathogenic inflammation in pancreatic cancer. *Nature* **623**, 415–422 (2023).
46. Z. Chen, L. Zhou, L. Liu, Y. Hou, M. Xiong, Y. Yang, J. Hu, K. Chen, Single-cell RNA sequencing highlights the role of inflammatory cancer-associated fibroblasts in bladder urothelial carcinoma. *Nat. Commun.* **11**, 5077 (2020).
47. M. Nowak, M. Klink, The role of tumor-associated macrophages in the progression and chemoresistance of ovarian cancer. *Cells* **9**, 1299 (2020).
48. Y. Ye, Q. Hu, H. Chen, K. Liang, Y. Yuan, Y. Xiang, H. Ruan, Z. Zhang, A. Song, H. Zhang, L. Liu, L. Diao, Y. Lou, B. Zhou, L. Wang, S. Zhou, J. Gao, E. Jonasch, S. H. Lin, Y. Xia, C. Lin, L. Yang, G. B. Mills, H. Liang, L. Han, Characterization of hypoxia-associated molecular features to aid hypoxia-targeted therapy. *Nat. Metab.* **1**, 431–444 (2019).
49. M. Klug, S. Schmidhofer, C. Gebhard, R. Andreesen, M. Rehli, 5-Hydroxymethylcytosine is an essential intermediate of active DNA demethylation processes in primary human monocytes. *Genome Biol.* **14**, R46 (2013).
50. F. Delhommeau, S. Dupont, V. Della Valle, C. James, S. Trannoy, A. Massé, O. Kosmider, J.-P. Le Couedic, F. Robert, A. Alberdi, Y. Lécluse, I. Plo, F. J. Dreyfus, C. Marzac, N. Casadevall, C. Lacombe, S. P. Romana, P. Dessen, J. Soulier, F. Viguié, M. Fontenay, W. Vainchenker, O. A. Bernard, Mutation in TET2 in myeloid cancers. *N. Engl. J. Med.* **360**, 2289–2301 (2009).
51. R. Matuleviciute, P. P. Cunha, R. S. Johnson, I. P. Foskolou, Oxygen regulation of TET enzymes. *FEBS J.* **288**, 7143–7161 (2021).
52. A. Casazza, D. Laoui, M. Wenes, S. Rizzolio, N. Bassani, M. Mambretti, S. Deschoemaeker, J. A. Van Ginderachter, L. Tamagnone, M. Mazzone, Impeding macrophage entry into hypoxic tumor areas by Sema3A/Nrp1 signaling blockade inhibits angiogenesis and restores antitumor immunity. *Cancer Cell* **24**, 695–709 (2013).
53. A. Sattiraju, S. Kang, B. Giotti, Z. Chen, V. J. Marallano, C. Brusco, A. Ramakrishnan, L. Shen, A. M. Tsankov, D. Hambardzumyan, R. H. Friedel, H. Zou, Hypoxic niches attract and sequester tumor-associated macrophages and cytotoxic T cells and reprogram them for immunosuppression. *Immunity* **56**, 1825–1843.e6 (2023).
54. A. Ohradanova-Repic, C. Machacek, C. Charvet, F. Lager, D. Le Roux, R. Platzer, V. Leksa, G. Mitulovic, T. R. Burkard, G. J. Zlabinger, M. B. Fischer, V. Feuillet, G. Renault, S. Blüml, M. Benko, M. Suchanek, J. B. Huppa, T. Matsuyama, A. Cavaco-Paulo, G. Bismuth, H. Stockinger, Extracellular purine metabolism is the switchboard of immunosuppressive macrophages and a novel target to treat diseases with macrophage imbalances. *Front. Immunol.* **9**, 852 (2018).
55. A.-T. Henze, M. Mazzone, The impact of hypoxia on tumor-associated macrophages. *J. Clin. Invest.* **126**, 3672–3679 (2016).
56. J. Jantsch, M. Wiese, J. Schödel, K. Castiglione, J. Gläsner, S. Kolbe, D. Mole, U. Schleicher, K.-U. Eckardt, M. Hensel, R. Lang, C. Bogdan, M. Schnare, C. Willam, Toll-like receptor activation and hypoxia use distinct signaling pathways to stabilize hypoxia-inducible factor 1α (HIF1A) and result in differential HIF1A-dependent gene expression. *J. Leukoc. Biol.* **90**, 551–562 (2011).
57. A. F. McGettrick, L. A. J. O'Neill, The role of HIF in immunity and inflammation. *Cell Metab.* **32**, 524–536 (2020).
58. X. Ke, C. Chen, Y. Song, Q. Cai, J. Li, Y. Tang, X. Han, W. Qu, A. Chen, H. Wang, G. Xu, D. Liu, Hypoxia modifies the polarization of macrophages and their inflammatory microenvironment, and inhibits malignant behavior in cancer cells. *Oncol. Lett.* **18**, 5871–5878 (2019).
59. D. G. DeNardo, D. J. Brennan, E. Rexhepaj, B. Ruffell, S. L. Shiao, S. F. Madden, W. M. Gallagher, N. Wadhwani, S. D. Keil, S. A. Junaid, H. S. Rugo, E. S. Hwang, K. Jirström, B. L. West, L. M. Coussens, Leukocyte complexity predicts breast cancer survival and functionally regulates response to chemotherapy. *Cancer Discov.* **1**, 54–67 (2011).
60. X. Xiang, J. Wang, D. Lu, X. Xu, Targeting tumor-associated macrophages to synergize tumor immunotherapy. *Signal Transduct. Target. Ther.* **6**, 75 (2021).
61. A. Mantovani, P. Allavena, F. Marchesi, C. Garlanda, Macrophages as tools and targets in cancer therapy. *Nat. Rev. Drug Discov.* **21**, 799–820 (2022).
62. R.-Y. Ma, A. Black, B.-Z. Qian, Macrophage diversity in cancer revisited in the era of single-cell omics. *Trends Immunol.* **43**, 546–563 (2022).
63. E. M. Wolf, B. Fingleton, A. H. Hasty, The therapeutic potential of TREM2 in cancer. *Front. Oncol.* **12**, 984193 (2022).
64. T.-L. Tang-Huau, P. Gueguen, C. Goudot, M. Durand, M. Bohec, S. Baulande, B. Pasquier, S. Amigorena, E. Segura, Human in vivo-generated monocyte-derived dendritic cells and macrophages cross-present antigens through a vacuolar pathway. *Nat. Commun.* **9**, 2570 (2018).
65. O. Morante-Palacios, L. Ciudad, R. Micheroli, C. Calle-Fabregat, T. Li, G. Barbisan, M. Houtman, S. G. Edalat, M. Frank-Bertoncelj, C. Ospelt, E. Ballestar, Coordinated glucocorticoid receptor and MAFB action induces tolerogenesis and epigenome remodeling in dendritic cells. *Nucleic Acids Res.* **50**, 108–126 (2022).
66. C. de la Calle-Fabregat, E. Niemantsverdriet, J. D. Cañete, T. Li, A. H. M. van der Helm-van Mil, J. Rodríguez-Ubreva, E. Ballestar, Prediction of the progression of undifferentiated arthritis to rheumatoid arthritis using DNA methylation profiling. *Arthritis Rheumatol.* **73**, 2229–2239 (2021).
67. C. de la Calle-Fabregat, J. Rodríguez-Ubreva, L. Ciudad, J. Ramírez, R. Celis, A. B. Azuaga, A. Cuervo, E. Graell, C. Pérez-García, C. Díaz-Torné, G. Salvador, J. A. Gómez-Puerta, I. Haro, R. Sanmartí, J. D. Cañete, E. Ballestar, The synovial and blood monocyte DNA methylomes mirror prognosis, evolution, and treatment in early arthritis. *JCI Insight* **7**, e158783 (2022).
68. S. Heinz, C. Benner, N. Spann, E. Bertolino, Y. C. Lin, P. Laslo, J. X. Cheng, C. Murre, H. Singh, C. K. Glass, Simple combinations of lineage-determining transcription factors prime cis-regulatory elements required for macrophage and B cell identities. *Mol. Cell* **38**, 576–589 (2010).
69. C. Y. McLean, D. Bristor, M. Hiller, S. L. Clarke, B. T. Schaar, C. B. Lowe, A. M. Wenger, G. Bejerano, GREAT improves functional interpretation of cis-regulatory regions. *Nat. Biotechnol.* **28**, 495–501 (2010).
70. J. M. Fernández, V. de la Torre, D. Richardson, R. Royo, M. Puiggròs, V. Moncunill, S. Fragkogianni, L. Clarke; BLUEPRINT Consortium, P. Flicek, D. Rico, D. Torrents, E. C. de Santa Pau, A. Valencia, The BLUEPRINT Data Analysis Portal. *Cell Syst.* **3**, 491–495.e5 (2016).
71. S. Andrews, FASTQC: A quality control tool for high throughput sequence data. (2010); www.bioinformatics.babraham.ac.uk/projects/fastqc.
72. P. Ewels, M. Magnusson, S. Lundin, M. Käller, MultiQC: Summarize analysis results for multiple tools and samples in a single report. *Bioinformatics* **32**, 3047–3048 (2016).
73. N. L. Bray, H. Pimentel, P. Melsted, L. Pachter, Near-optimal probabilistic RNA-seq quantification. *Nat. Biotechnol.* **34**, 525–527 (2016).
74. C. Soneson, M. I. Love, M. D. Robinson, Differential analyses for RNA-seq: Transcript-level estimates improve gene-level inferences. *F1000Res.* **4**, 1521 (2015).
75. M. I. Love, W. Huber, S. Anders, Moderated estimation of fold change and dispersion for RNA-seq data with DESeq2. *Genome Biol.* **15**, 550 (2014).
76. G. Yu, L.-G. Wang, Y. Han, Q.-Y. He, clusterProfiler: An R package for comparing biological themes among gene clusters. *Omics J. Integr. Biol.* **16**, 284–287 (2012).
77. M. Martin, Cutadapt removes adapter sequences from high-throughput sequencing reads. *EMBnet.journal* **17**, 10 (2011).
78. H. Li, Aligning sequence reads, clone sequences and assembly contigs with BWA-MEM. arXiv: 1303.3997 [q-bio.GN] (2013); http://arxiv.org/abs/1303.3997).
79. H. Li, B. Handsaker, A. Wysoker, T. Fennell, J. Ruan, N. Homer, G. Marth, G. Abecasis, R. Durbin; 1000 Genome Project Data Processing Subgroup, The sequence alignment/map format and SAMtools. *Bioinformatics* **25**, 2078–2079 (2009).
80. H. M. Amemiya, A. Kundaje, A. P. Boyle, The ENCODE Blacklist: Identification of problematic regions of the genome. *Sci. Rep.* **9**, 9354 (2019).
81. F. Ramírez, D. P. Ryan, B. Grüning, V. Bhardwaj, F. Kilpert, A. S. Richter, S. Heyne, F. Dündar, T. Manke, deepTools2: A next generation web server for deep-sequencing data analysis. *Nucleic Acids Res.* **44**, W160–W165 (2016).
82. Y. Zhang, T. Liu, C. A. Meyer, J. Eeckhoute, D. S. Johnson, B. E. Bernstein, C. Nusbaum, R. M. Myers, M. Brown, W. Li, X. S. Liu, Model-based analysis of ChIP-Seq (MACS). *Genome Biol.* **9**, R137 (2008).
83. Bioconductor, DiffBind (development version), http://bioconductor.org/packages/DiffBind.
84. M. Lawrence, W. Huber, H. Pagès, P. Aboyoun, M. Carlson, R. Gentleman, M. T. Morgan, V. J. Carey, Software for computing and annotating genomic ranges. *PLOS Comput. Biol.* **9**, e1003118 (2013).
85. A. M. Newman, C. B. Steen, C. L. Liu, A. J. Gentles, A. A. Chaudhuri, F. Scherer, M. S. Khodadoust, M. S. Esfahani, B. A. Luca, D. Steiner, M. Diehn, A. A. Alizadeh, Determining cell type abundance and expression from bulk tissues with digital cytometry. *Nat. Biotechnol.* **37**, 773–782 (2019).
86. Z. Gu, R. Eils, M. Schlesner, Complex heatmaps reveal patterns and correlations in multidimensional genomic data. *Bioinformatics* **32**, 2847–2849 (2016).
87. S. Jin, M. V. Plikus, Q. Nie, CellChat for systematic analysis of cell-cell communication from single-cell and spatially resolved transcriptomics. bioRxiv 2023.11.05.565674 [Preprint] (2023). https://doi.org/10.1101/2023.11.05.565674.
88. Á. Nagy, G. Munkácsy, B. Győrffy, Pancancer survival analysis of cancer hallmark genes. *Sci. Rep.* **11**, 6047 (2021).
89. Y. Li, D. Ge, C. Lu, The SMART App: An interactive web application for comprehensive DNA methylation analysis and visualization. *Epigenetics Chromatin* **12**, 71 (2019).
90. V. Thorsson, D. L. Gibbs, S. D. Brown, D. Wolf, D. S. Bortone, T.-H. O. Yang, E. Porta-Pardo, G. F. Gao, C. L. Plaisier, J. A. Eddy, E. Ziv, A. C. Culhane, E. O. Paull, I. K. A. Sivakumar, A. J. Gentles, R. Malhotra, F. Farshidfar, A. Colaprico, J. S. Parker, L. E. Mose, N. S. Vo, J. Liu, Y. Liu, J. Rader, V. Dhankani, S. M. Reynolds, R. Bowlby, A. Califano, A. D. Cherniack, D. Anastassiou, D. Bedognetti, Y. Mokrab, A. M. Newman, A. Rao, K. Chen, A. Krasnitz, H. Hu, T. M. Malta, H. Noushmehr, C. S. Pedamallu, S. Bullman, A. I. Ojesina, A. Lamb, W. Zhou, H. Shen, T. K. Choueiri, J. N. Weinstein, J. Guinney, J. Saltz, R. A. Holt, C. S. Rabkin; Cancer Genome Atlas Research Network, A. J. Lazar, J. S. Serody, E. G. Demicco, M. L. Disis, B. G. Vincent, I. Shmulevich, The immune landscape of cancer. *Immunity* **48**, 812–830.e14 (2018).
91. Y. Tang, M. Horikoshi, W. Li, ggfortify: Unified interface to visualize statistical results of popular R packages. *R J.* **8**, 474–485 (2016).

92. F. Hahne, R. Ivanek, in *Statistical Genomics*, vol 1418 of Methods in Molecular Biology, E. Mathé, S. Davis, Eds. (Springer, 2016), pp. 335–351.
93. S. Kurtenbach, J. William Harbour, SparK: A publication-quality NGS visualization tool. bioRxiv 845529 [Preprint] (2019). https://doi.org/10.1101/845529.

Acknowledgments: We would like to thank M. A. Fernández from the cytometry core facility at the Germans Trias i Pujol Institute (IGTP) for help with flow cytometry, J. G. Bessa from the microscopy unit of Josep Carreras Institute (IJC) for the aid during confocal microscopy analyses, F. Berthou from the imaging and cytometry platform (PFIC/UMS AMMICa) at Gustave Roussy (GR) for helping with the FACS cell sorting, and Life & Brain GmbH for the generation of DNA methylation and gene expression data (RNA-seq). **Funding:** This study was supported by the CERCA Programme/Generalitat de Catalunya and the Josep Carreras Foundation for institutional support. E.B. was funded by the Spanish Ministry of Science and Innovation (PID2020-117212RB-I00; AEI/10.13039/501100011033) and the Agency for Management of University and Research Grants (AGAUR; 2021 SGR 01213). **Author contributions:** Conceptualization: C.d.l.C.-F., J.C.-S., Á.L.C., J.R.-U., F.G., and E.B. Methodology: C.d.l.C.-F., J.C.-S., M.G., L.C., A.S., and E.B. Software: C.d.l.C.-F., J.C.-S., and K.M. Validation: C.d.l.C.-F., J.C.-S., G.D., L.C., S.G., and E.B. Formal analysis: C.d.l.C.-F., J.C.-S., A.S., and S.G. Investigation: C.d.l.C.-F., J.C.-S., M.G., and G.D. Resources: L.C., J.M.-C., C.M.-P., and J.M. Data curation: C.d.l.C.-F. and J.C.-S. Writing (original draft): C.d.l.C.-F., J.C.-S., L.C., and E.B. Writing (review and editing): C.d.l.C.-F., J.C.-S., C.M.-P., J.R.-U., F.G., and E.B. Visualization: C.d.l.C.-F. and J.C.-S. Supervision: C.-A.D. and E.B. Project administration: C.-A.D., J.R.-U., F.G., and E.B. Funding acquisition: E.B. **Competing interests:** The authors declare that they have no competing interests. **Data and materials availability:** DNA methylation, RNA-seq, and ChIP-seq datasets for this publication have been deposited in the NCBI Gene Expression Omnibus and are accessible through GEO SuperSeries accession number GSE261324. Previously published data analyzed here are available through the following identifiers or directions: ftp.ebi.ac.uk/pub/databases/blueprint (ChIP-seq), GSE156921 (RNA-seq), and github.com/gustaveroussy/FG-Lab (*10*) (scRNA-seq). All other data needed to evaluate the conclusions in the paper are present within the manuscript, figures, or the Supplementary Materials.

Submitted 17 May 2024
Accepted 12 August 2024
Published 18 September 2024
10.1126/sciadv.adq5226